https://doi.org/10.5194/egusphere-2022-1388
Preprint. Discussion started: 2 January 2023

Seismic wave modeling of fluid-saturated fractured porous rock: Including fluid pressure diffusion effects of discrete distributed large-scale fractures

Yingkai Qi[1,2], Xuehua Chen[1,2], Qingwei Zhao[1,2], Xin Luo[1], Chunqiang Feng[3]

[1]State Key Laboratory of Oil & Gas Reservoir Geology and Exploitation, Chengdu University of Technology, Chengdu, 610059, China

[2]Key Laboratory of Earth Exploration & Information Techniques of Ministry of Education, Chengdu University of Technology, Chengdu, 610059, China

[3]Exploration & Development Research Institute of Henan Oilfield, Sinopec, 473000, China

Correspondence to: Xuehua Chen (chen_xuehua@163.com)

Abstract. The scattered seismic waves of fractured porous rock are strongly affected by the wave-induced fluid pressure diffusion effects between the compliant fractures and the stiffer embedding background. To include these poroelastic effects in seismic modeling, we develop a numerical scheme for discrete distributed large-scale fractures embedded in fluid-saturated porous rock. Using Coates and Schoenberg's local effective medium theory and Barbosa's dynamic linear slip model characterized by complex-valued and frequency-dependent fracture compliances, we derive the effective viscoelastic compliances in each spatial discretized cell by superimposing the compliances of the background and the fractures. The effective governing equations of the fractured porous rock are then characterized by the derived anisotropic, complex-valued, and frequency-dependent effective compliances. We numerically solved the effective governing equations by mixed-grid stencil frequency-domain finite-difference method. The good consistency between the scattered waves off a single horizontal fracture calculated using our proposed scheme and those calculated using the poroelastic linear slip model shows that our modeling scheme can properly include the FPD effects. We also find that for a P-point source, the amplitudes of the scattered waves from a single horizontal fracture are strongly affected by the fluid stiffening effects due to fluid pressure diffusion, while for an S-point source, the scattered waves are less sensitive to fluid pressure diffusion. In the case of the conjugate fracture system, the scattered waves from the bottom of the fractured reservoir and the reflected waves from the underlying formation are attenuated and dispersed by the FPD effects for both P- and S-point sources. The proposed numerical modeling scheme can also be used to improve migration quality and the estimation of fracture mechanical characteristics in inversion.

1 Introduction

Fluid saturated porous rock in the reservoir characterized by a heterogeneous internal structure consisting of a solid skeleton and interconnected fluid-filled voids, are often permeated by much more compliant and permeable fractures. Although the fractures typically occupy only a small volume, they tend to dominate the overall mechanical and hydraulic properties of the reservoir (Liu et al., 2000; Gale et al., 2014). Thus, fracture detection, characterization and imaging are of great importance for reservoir prediction and production. Seismic waves are widely used for these purposes because their behaviors (amplitude, phase and anisotropy) are strongly affected by the fractures (Chapman, 2003; Gurevich, 2003; Brajanovski et al., 2005; Carcione et al., 2011; Rubino et al., 2014). Therefore, appropriate numerical modeling methods are required for the interpretation, migration and inversion of seismic data from porous media containing discrete distributed fractures.

Biot's poroelastic theory (Biot, 1956a; b) is the fundamental theory to describe elastic wave propagation in fluid porous media, including the dynamic interactions between rock and pore fluid. However, the original theory, assuming a macroscopically homogeneous porous media saturated by a single fluid phase, is fail to explain the measured velocity dispersion and attenuation of seismic waves (Nakagawa et al., 2007). In recent decades, many researchers found that if porous media contains mesoscale heterogeneity (ignored by Boit), a local fluid-pressure gradient will be induced by the passing wave at scale comparable to the wave-induced fluid pressure diffusion length (the wavelength of slow P-wave), causing significant velocity dispersion and velocity attenuation at seismic frequency band (White et al., 1975; Dutta and Odé, 1979; Johnson, 2001; and Müller et al. 2008; Norris, 1993; Gurevich et al., 1997; Gelinsky and Shapiro, 1997; Kudarova et al., 2016). Fractures embedded in homogeneous porous background are special heterogeneities, exhibiting strong mechanical contrasts with background. When seismic waves travel through fluid saturated fractured porous rocks, local fluid pressure gradients will be induced between the fractures and the background in response to the strong compressibility contrast. To return the equilibrium state, fluid pressure diffusion (FPD) occurs between the fractures and the embedding background, which in turn changes the fluid stiffening effect on the fractures and thus their mechanical compliances depending on frequency (Barbosa et al., 2016a, b).

When fractures with apertures and lengths much smaller than the wavelengths are unified distributed in porous rock, the properties of fractured rock are homogeneous at macroscopic scale and can be described by a representative elementary volume (REV). Various effective medium theories are available for estimating the fracture-induced anisotropy, attenuation and dispersion behaviors (Hudson, 1981; Thomsen, 1995; Chapman, 2003; Brajanovski et al., 2005; Krzikalla et al. 2011; Galvin et al., 2015; Guo et al., 2017a; b). The discrete distributed large-scale fractures (the presence of spatial correlations of fractures), however, cannot be modeled by any above-mentioned effective medium theories originally for macroscopically uniformly distributed fractures. The seismic response of individual fracture is mostly assessed in the framework of the linear slip model (LSM) by modeling a fracture as a nonwelded interface across which the displacement tensors are assumed to be discontinuous while the stress tensors are continuous (Schoenberg, 1980). Various local numerical schemes have been developed for discrete distributed large-scale fractures. The most widely used scheme is local effective-medium schemes (Coates and Schoenberg, 1995; Igel et al., 1997; Vlastos et al., 2003; Oelke, et al., 2013) that determine and incorporate the behavior of fracture-induced media within each spatial discretized cell. The advantage of using the local effective medium is that it requires no special treatment of the displacement discontinuity conditions on the fractures. An alternative scheme is the explicit interface scheme that directly treat the displacement discontinuity across each fracture (Zhang, 2005; Cui et al., 2018; Khokhlov, et al., 2021).

https://doi.org/10.5194/egusphere-2022-1388
Preprint. Discussion started: 2 January 2023

The common aspect of the aforementioned numerical modeling schemes is that they are all implemented in a purely elastic framework with real-valued compliances boundary and represent both the embedding background and factures as elastic solids, thus the impact of FPD effects on seismic scattering can't be accounted for. A dynamic linear slip model incorporating FPD effects should be considered when implementing numerical modeling of seismic wave propagating in fluid saturated porous rocks containing discrete distributed large-scale fractures. Rubino et al. (2015) proposed a frequency-dependent complex-valued normal compliance for regularly distributed planar fractures (a set of aligned fractures) with a separation much smaller than the prevailing seismic wavelength. Despite the ability of including the FPD across the fractures, the model is not suitable for modeling discrete distributed fractures. Nakagawa and Schoenberg (2007) developed an extended LSM for a single fracture in the context of poroelasticity. The proposed model representing both the background and the fracture as poroelastic media can appropriately incorporate the frequency related effects, but it will also result in a higher computational consuming and more memory requirements. In the context of viscoelasticity, Barbosa et al. (2016a) developed a viscoelastic linear slip model (VLSM) for an individual fracture with explicit complex-valued and frequency-dependent fracture compliances, to account for the impact of FPD on the fracture stiffness. That provides a viscoelasticity-based modeling algorithm for discrete distributed large-scale fractures with smaller computational costs and memory requirements than the poroelasticity based modeling.

In this paper, we develop a viscoelastic numerical modeling scheme to simulate seismic wave propagation in fluid-saturated porous media containing discrete distributed large-scale fractures. To capture the FPD effects between the fractures and background, we use the local effective medium theory based on Barbosa's VLSM to derive the effective anisotropic viscoelastic compliances in each numerical cell by superimposing the compliances of the background and the fractures. The effective anisotropic viscoelastic governing equations of the fractured porous rock are then numerically solved using mixed-grid stencil frequency-domain finite-difference method (FDFD) (Hustedt, et al. 2004; Operto, et al. 2009; Liu et al., 2018). To validate the proposed viscoelastic modeling scheme can capture the impact of FPD effects on seismic wave scattering, we compare the scattered waves of a single horizontal fracture obtained using our proposed modeling scheme with those obtained using poroelastic modeling scheme and elastic modeling scheme. Numerical examples of a fractured reservoir are presented to demonstrate that the proposed modeling scheme can properly simulate the wave attenuation and dispersion due to the FPD effects between the fracture system and background. A complex modified Marmousi model is also use to test the proposed modeling scheme and code. The scheme can be used not only to study the impact of mechanical and hydraulic of fracture properties on seismic scattering but can also to improve migration quality and the estimation of fracture mechanical characteristics in inversion.

2 The elastic models

The two most widely used non-attenuated and non-dissipative elastic models for fractured porous media are the low- and high-frequency limits elastic LSM that ignore the FPD effects between the background and the fractures. The two elastic models can be used to determine the effective anisotropic-elastic-moduli of the fractured porous rock.

2.1 The low-frequency limits elastic linear slip models (LFLSM)

The presence of fractures in a homogeneous and isotropic porous rock results in an effective anisotropic medium. The effective compliance matrix of the dry fractured rock $\mathbf{S}^{dry}$ can be obtained using the LSM (Schoenberg and Sayers, 1995):

$$\mathbf{S}^{dry} = \mathbf{S}_b^{dry} + \mathbf{Z}_0, \tag{1}$$

where $\mathbf{S}_b^{dry}$ is the isotropic compliance matrix of the dry background medium in the absent of fractures, and $\mathbf{Z}_0$ is the excess compliance matrix due to the dry fractures. For a single set of rotationally invariant fractures, $\mathbf{Z}_0$ can be written as (Schoenberg and Sayers, 1995):

$$Z_{ij,0} = \frac{Z_T}{4}\left(\delta_{ik}n_l n_j + \delta_{jk}n_l n_i + \delta_{il}n_k n_j + \delta_{jl}n_k n_i\right) + \left(Z_{N_d} - Z_T\right)n_i n_j n_k n_l, \tag{2}$$

where n_i is the component of the local unit normal to the fracture surface, Z_{N_d} and Z_T are the drained normal fracture compliance and tangential fracture compliance, respectively, as functions of fracture thickness h^c and the drained longitudinal modulus H_d^c and shear moduli μ^c of the fracture (Brajanovski et al., 2005):

$$Z_{N_d} \equiv \frac{h^c}{H_d^c}, \quad Z_T \equiv \frac{h^c}{\mu^c}. \tag{3}$$

Since the fluid pressure is uniform in the low-frequency limit, the corresponding effective stiffness matrix $\mathbf{C}_{lf}^{\mathrm{sat}}$ of the fluid saturated rock can be obtained using the anisotropic Gassmann equation (Gurevich, 2003):

$$C_{ij,lf}^{\mathrm{sat}} = C_{ij}^{\mathrm{dry}} + \alpha_i\alpha_j M_{dry}, \quad i,j = 1,\ldots,6. \tag{4}$$

The anisotropic Biot-Willis coefficients α_m are:

$$\alpha_m = 1 - \frac{\sum_{n=1}^{3} C_{mn}^{\mathrm{dry}}}{3K_g}, \quad m = 1,2,3, \tag{5}$$

$\alpha_4 = \alpha_5 = \alpha_6 = 0$. The Biot's fluid-storage modulus M is

$$M_{dry} = \frac{K_g}{\left(1-K_0^*/K_g\right) - \phi\left(1-K_g/K_f\right)}, \tag{6}$$

where K_g denotes the grain solid bulk modulus, K_f the pore fluid bulk modulus, and K_0^* the generalized drained bulk modulus, defined as

$$K_0^* = \frac{1}{9}\sum_{i=1}^{3}\sum_{j=1}^{3} C_{ij}^{\mathrm{dry}}. \tag{7}$$

2.2 The high-frequency limits elastic linear slip models (HFLSM)

In the high-frequency limit, the fractures are hydraulically isolated from the saturated background medium. The effective compliance matrix of the saturated background medium permeated by the dry fractures can be expressed as (Guo et al., 2016):

$$\mathbf{S}_{hf}^{1} = \mathbf{S}_b^{sat} + \mathbf{Z}_0, \tag{8}$$

where $\mathbf{S}_b^{sat}$ is the isotropic compliance matrix of the saturated background medium in the absent of fractures. The effective stiffness coefficients of the saturated fractured rock can be written as:

$$C_{ij,hf}^{\text{sat}} = C_{ij,hf}^{1} + \alpha_i^1 \alpha_j^1 M_1, \quad i,j = 1, \dots, 6, \tag{9}$$

where α^1 and M_1 can be again calculated using Eqs. (5)-(7) but replacing the solid grains bulk modulus K_g with saturated bulk modulus of the background K_m^{sat}, the overall porosity ϕ with the fracture porosity ϕ_c.

3 Nakagawa's poroelastic LSM (PLSM)

Nakagawa and Schoenberg (2007) presented a PLSM in the framework of poroelasticity, representing the fracture as a highly compliant and porous thin layer embedded in a much stiffer and much less porous background (Barbosa et al., 2016a). Similar to the classic LSM, the PLSM assumes that across a fracture surface the stress tensor is continuous while the displacement tensor is discontinuous. The discontinuous displacement components for a horizonal fracture are (Nakagawa and Schoenberg, 2007):

$$[u_x] = Z_T \tau_{xz}, \tag{10a}$$

$$[u_y] = Z_T \tau_{yz}, \tag{10b}$$

$$[u_z] = Z_{N_D}(\tau_{zz} + \alpha P_f), \tag{10c}$$

$$[w_z] = -\alpha Z_{N_D}\left(\tau_{zz} + \frac{1}{B} P_f\right), \tag{10d}$$

where the parameter $B = \alpha M / H_u$, and the definition of drained normal fracture compliance Z_{N_D} and tangential fracture compliance Z_T are the same as those in LFLEM. Since the PLSM represents both the background and the fracture as poroelasticity, it is capable to describe the discontinuous displacement of the relative fluid in addition to the solid, implying that it can properly handle the FPD effects between the background and the fracture. Although it is difficult to incorporate the PLSM into the effective medium theory to obtain the effective moduli of the fractured porous rock, these boundary conditions can be easily incorporated into poroelastic finite-difference algorithm for modeling seismic wave scattering off large-scale fractures parallel to the coordinate axis. An alternative wavenumber domain method for modeling the scattered waves by poroelastic fractures is presented by Nakagawa and Schoenberg (2007) based on the PLSM.

4 Barbosa's viscoelastic LSM (VLSM)

Barbosa et al. (2016a) derived a VLSM that account for the FPD effects between a fracture and background and the resulting stiffening effect impact on the fracture. The background is assumed to be not impacted by the FPD and can be represented by an elastic solid, whose properties are computed according to Gassmann's equation. By representing fractures as extremely thin viscoelastic layers, the poroelastic effects were incorporated into the classical LSM through complex-valued and frequency-dependent compliances. These compliances characterize the mechanical properties of the fluid-saturated fracture.

4.1 The boundary conditions of VLSM

The discontinuous displacement components of the VLSM (Barbosa et al., 2016a) for a horizontal fracture are

$$[u_x] = Z_T \tau_{xz}, \tag{11a}$$

$$[u_y] = Z_T \tau_{yz}, \tag{11b}$$

$$[u_z] = Z_N \tau_{zz} + Z_X \varepsilon_{xx}, \tag{11c}$$

where Z_N and Z_T are generalized normal and tangential compliances respectively, and Z_X is related to the coupling between horizontal and vertical deformation of the fracture. The normal compliance Z_N and additional parameter Z_X are complex-valued and frequency-dependent, while the tangential compliance Z_T is the same as for elastic and poroelastic models. The three effective fracture parameters are given by Barbosa et al. (2016a)

$$\eta_N = \frac{\eta_{N_D}\left[\alpha \eta_{N_U} D_{P_2}^b - 2B\gamma_{P_2}^b ik_{P_2}^b - 2\alpha ik_{P_2}^b\left(1/\gamma_{P_2}^b + 2B\right)\right]}{\alpha \eta_{N_D} D_{P_2}^b - 2B\gamma_{P_2}^b ik_{P_2}^b}, \tag{12a}$$

$$\eta_X = \frac{-4k_{P_2}^b \alpha^b \eta_T M^b \mu^b \mu\left(\alpha H_U^b M - \alpha^b H_U M^b\right)}{\left(H_U^b\right)^2\left(hH_U \omega \eta_f^b + 2k_{P_2}^b M H_D \kappa^b\right)}. \tag{12b}$$

We rewrite Eqs. (12a)-(12b) as

$$Z_N = Z_{N_U} + Z_{N_D}\frac{G_1(1+i)}{\sqrt{\omega} + G_2(1+i)}, \tag{13a}$$

$$Z_X = -\frac{G_3(1+i)}{\sqrt{\omega} + G_4(1+i)}, \tag{13b}$$

where Z_{N_U} and Z_{N_D} are the undrained and drained normal fracture compliance respectively, ω is the angular frequency. The four real-valued parameters G_1, G_2, G_3 and G_4 are defined as

$$G_1 = \sqrt{\frac{\kappa^b}{\eta N^b}}\frac{\left(B^b - B^c\right)^2}{\eta_{N_D}}, \qquad G_2 \approx \sqrt{\frac{\kappa^b}{\eta N^b}}\frac{1}{\eta_{N_D}}, \tag{14a}$$

$$G_3 = \frac{2\sqrt{2}\,\alpha^b \mu^b \left(B^b - B^c\right)\sqrt{D^b}}{H_D^b}, \quad G_4 = \frac{\sqrt{2}\,\kappa^b}{h^c \kappa^c}\frac{D^c}{\sqrt{D^b}}, \tag{14b}$$

where the parameters with superscripts b correspond to background properties and the parameters with superscripts c correspond to fracture parameters. In Eqs. (14a)-(14b), D is the diffusivity defined as $D = \kappa N/\eta$ ($N = H_D M/H_U$), and the dimensionless parameter B defined as $B = \alpha M/H_U$. H_U, H_D and μ are the corresponding undrained P wave modulus, drained P wave modulus and shear modulus. The Barbosa's VLSM can properly capture the FPD effects between a fracture and background.

4.2 The effective viscoelastic-anisotropic stiffness matrix based on Barbosa's VLSM

To incorporate the VLSM into viscoelastic finite-difference modeling algorithms, we give the specific derivation of the effective viscoelastic-anisotropic stiffness matrix of the numerical grids on a fracture based on Coates and Schoenberg's local effective medium theory (1995). The porous background is assumed to be unaffected by the FPD in the presence of fractures because of the small amount of diffusing fluid and large compliance contrast between background and fluid. Thus, the rock background can be represented by an elastic homogeneous solid and the strain $\boldsymbol{\varepsilon}^b$ of the background can be expressed as

$$\varepsilon_{ij}^{b} = s_{ijkl}^{b}\sigma_{kl}, \tag{15}$$

where the compliance tensor $\mathbf{s}^b$ are computed according to Gassmann's equation (Rubino et al., 2015; Barbosa et al., 2016a), and $\boldsymbol{\sigma}$ is the average stress tensor. The exceed strain tensor $\boldsymbol{\varepsilon}^c$ induced by a single fracture with surface S in a representative volume V (e.g. the volume of numerical cell) is given by (Hudson and Knopoff, 1989; Sayers and Kachanov, 1995; Liu, et al., 2000)

$$\varepsilon_{ij}^{c} = s_{ijkl}^{c}\sigma_{kl} = \frac{1}{2V}\int\left([u_i]n_j + [u_j]n_i\right)dS, \tag{16}$$

where $\boldsymbol{s}^c$ is the extra compliance tensor resulting from the fractures, $[u_i]$ is the ith component of the displacement discontinuity on S and n_i is the ith component of the fracture normal. Note that Eq. (16) is applicable to finite, nonplanar fractures in the long wavelength limit, i.e., the applied stress is assumed to be constant over the representative volume.

If we assume that the interface of the fracture is normal to the z-axis (fracture normal vector $\boldsymbol{n}$ is (0,0,1)), substituting Eqs. (11a)-(11c) into Eq. (16), we can obtain the nonzero element of the exceed fracture strain tensor

$$\varepsilon_{xz}^{c} = \frac{S}{V}Z_T\tau_{xz}, \tag{17a}$$

$$\varepsilon_{yz}^{c} = \frac{S}{V}Z_T\tau_{yz}, \tag{17b}$$

$$\varepsilon_{zz}^{c} = \frac{S}{V}\left(Z_N\tau_{zz} + Z_X\varepsilon_{xx}^{b}\right), \tag{17c}$$

Then the exceed fracture strain tensor ε_{ij}^{c} and the background strain tensor ε_{ij}^{b} can be written in matrix from in Voigt notation

$$\mathbf{e}^b = \mathbf{S}^b\boldsymbol{\sigma}, \tag{18}$$

$$\mathbf{e}^c = \frac{S}{V}\left(\mathbf{Z}_1\boldsymbol{\sigma} + \mathbf{Z}_2\mathbf{e}^b\right) = \frac{S}{V}\left(\mathbf{Z}_1 + \mathbf{Z}_2\mathbf{S}^b\right)\boldsymbol{\sigma}, \tag{19}$$

where the strain matrix $\mathbf{e} = [\varepsilon_{11}, \varepsilon_{22}, \varepsilon_{33}, 2\varepsilon_{23}, 2\varepsilon_{13}, 2\varepsilon_{13}]^T$, and the stress matrix $\boldsymbol{\sigma} = [\sigma_{11}, \sigma_{22}, \sigma_{33}, \sigma_{23}, \sigma_{13}, \sigma_{12}]^T$. The 6×6 fracture compliance matrix $\mathbf{Z}_1$ and additional dimensionless matrix $\mathbf{Z}_2$ according to the Voigt notation are defined as

$$\mathbf{Z}_1 = \begin{bmatrix} 0 & 0 & 0 & 0 & 0 & 0 \\ 0 & 0 & 0 & 0 & 0 & 0 \\ 0 & 0 & Z_N & 0 & 0 & 0 \\ 0 & 0 & 0 & Z_T & 0 & 0 \\ 0 & 0 & 0 & 0 & Z_T & 0 \\ 0 & 0 & 0 & 0 & 0 & 0 \end{bmatrix}, \quad \mathbf{Z}_2 = \begin{bmatrix} 0 & 0 & 0 & 0 & 0 & 0 \\ 0 & 0 & 0 & 0 & 0 & 0 \\ Z_X & 0 & 0 & 0 & 0 & 0 \\ 0 & 0 & 0 & 0 & 0 & 0 \\ 0 & 0 & 0 & 0 & 0 & 0 \\ 0 & 0 & 0 & 0 & 0 & 0 \end{bmatrix}. \tag{20}$$

The average strain $\mathbf{e}$ in a homogeneous porous rock containing single fracture can be expressed as the sum of the strains of background and the fractures

$$\mathbf{e} = \mathbf{e}^b + \mathbf{e}^c. \tag{21}$$

Substituting Eq. (15) and Eq. (19) into Eq. (21), we can obtain the average strain matrix

$$\mathbf{e} = \left[\mathbf{S}^b + \frac{S}{V}\left(\mathbf{Z}_1 + \mathbf{Z}_2\mathbf{S}^b\right)\right]\boldsymbol{\sigma}. \tag{22}$$

Thus, the effective stiffness matrix $\mathbf{C}$ can be expressed as

$$\mathbf{C} = \left[\mathbf{S}^b + \frac{S}{V}\left(\mathbf{Z}_1 + \mathbf{Z}_2\mathbf{S}^b\right)\right]^{-1} = \mathbf{C}^b\left[\mathbf{I} + \frac{S}{V}\left(\mathbf{Z}_1\mathbf{C}^b + \mathbf{Z}_2\right)\right]^{-1}. \tag{23}$$

https://doi.org/10.5194/egusphere-2022-1388
Preprint. Discussion started: 2 January 2023

The effective stiffness matrix of case of an inclined fracture can be obtained by rotating the coordinate axis to keep z-axis perpendicular to fracture interface. We first define the inclined fracture have an angle φ and an azimuth angle θ, and then the rotation matrix can be obtained:

$$\mathbf{R} = \begin{bmatrix} cos\theta cos\varphi & -sin\theta & cos\theta sin\varphi \\ sin\theta cos\varphi & cos\theta & sin\theta sin\varphi \\ -sin\varphi & 0 & cos\varphi \end{bmatrix}, \tag{24}$$

as well as the corresponding stress Bond matrix $\mathbf{A}_\sigma$ and strain Bond matrix $\mathbf{A}_\varepsilon$. The new stress matrix $\mathbf{e}'$ and strain matrix $\boldsymbol{\sigma}'$ can be expressed as the multiplication of the old one and Bond matrix

$$\mathbf{e}' = \mathbf{A}_\varepsilon \mathbf{e} \;\; , \;\; \boldsymbol{\sigma}' = \mathbf{A}_\sigma \boldsymbol{\sigma}. \tag{25}$$

By substituting Eq. (25) into Eq. (19), the new exceed fracture strain matrix can be obtained

$$\mathbf{e}^c = \frac{S}{V}\mathbf{A}_\varepsilon(\mathbf{Z}_1 + \mathbf{Z}_2\mathbf{S}^b)\mathbf{A}_\varepsilon^T\boldsymbol{\sigma}. \tag{26}$$

Finally, substituting Eq. (6) into Eq. (21), the average strain matrix of each numerical cell containing discrete distributed fractures with the same arbitrary direction can be expressed as

$$\mathbf{e} = \left[\boldsymbol{S}^b + \frac{S}{V}\mathbf{A}_\varepsilon(\mathbf{Z}_1 + \mathbf{Z}_2\boldsymbol{S}^b)\mathbf{A}_\varepsilon^T\right]\boldsymbol{\sigma}, \tag{27}$$

and the corresponding effective stiffness matrix $\mathbf{C}$ is

$$\mathbf{C} = \left[\boldsymbol{S}^b + \frac{S}{V}\mathbf{A}_\varepsilon(\mathbf{Z}_1 + \mathbf{Z}_2\boldsymbol{S}^b)\mathbf{A}_\varepsilon^T\right]^{-1}, \tag{28}$$

If the background media is isotropic, the $\mathbf{C}$ can be simplified as

$$\mathbf{C} = \mathbf{C}^b\left[\mathbf{I} + \frac{S}{V}\mathbf{A}_\varepsilon(\mathbf{Z}_1\mathbf{C}^b + \mathbf{Z}_2)\mathbf{A}_\varepsilon^T\right]^{-1}, \tag{29}$$

If we ignore the interaction between different fractures and the FPD along the fracture interfaces, the result can be easily extended to the case of multiple sets of discrete distributed large-scale fractures with arbitrary orientation:

$$\mathbf{C} = \mathbf{C}^b\left[\mathbf{I} + \sum_{r=1}^{N_c}\frac{S_r}{V}\mathbf{A}_{\varepsilon r}(\mathbf{Z}_{1r}\mathbf{C}^b + \mathbf{Z}_{2r})\mathbf{A}_{\varepsilon r}^T\right]^{-1}, \tag{30}$$

where N_c is total number of the fracture directions and the subscript r denotes the rth direction. The derived effective stiffness matrix is to be employed in the viscoelastic finite-difference modeling of discrete distributed large-scale fractures in porous rock.

5. Seismic modeling of fractured porous rock

In this section, we focus on the implementation of seismic modeling of fluid-saturated porous media containing discrete distributed large-scale fractures in 2D case. We develop a viscoelastic modeling scheme based on the VLSM and local effective medium theory (Coates and Schoenberg, 1995) to incorporate the FPD effects between fractures and background. To validate that the proposed viscoelastic modeling scheme can capture the impact of FPD effects on seismic wave scattering of fractures, we outline the implementation of poroelastic modeling scheme using an explicit application of the PLSM.

https://doi.org/10.5194/egusphere-2022-1388
Preprint. Discussion started: 2 January 2023

5.1 viscoelastic modeling based on VLSM

For viscoelastic modeling, we adopt local effective media theory based on VLSM to derive the effective anisotropic viscoelastic compliances in each numerical cell by superimposing the compliances of the background and the fractures. Since the real structure of the rock is substituted by ideally continua, the balance equations of classical continuum mechanics can be applied without considering the discontinuity at the fracture interfaces (Lewis and Schrefler, 1998; Gavagnin et al., 2020), and the constitutive equations are characterized by effective complex-valued and frequency-dependent TTI viscoelastic stiffness. Thus, the second-order heterogeneous governing equations of fractured porous rock with PML in frequency domain can be expressed as:

$$\omega^2\rho u_x + \frac{1}{\xi_x}\partial_x\left(\frac{c_{11}}{\xi_x}\partial_x u_x + \frac{c_{13}}{\xi_z}\partial_z u_z + \frac{c_{15}}{\xi_z}\partial_z u_x + \frac{c_{15}}{\xi_x}\partial_x u_z\right) + \frac{1}{\xi_z}\partial_z\left(\frac{c_{15}}{\xi_x}\partial_x u_x + \frac{c_{35}}{\xi_z}\partial_z u_z + \frac{c_{55}}{\xi_z}\partial_z u_x + \frac{c_{55}}{\xi_x}\partial_x u_z\right) = 0, \quad (31a)$$

$$\omega^2\rho u_z + \frac{1}{\xi_x}\partial_x\left(\frac{c_{15}}{\xi_x}\partial_x u_x + \frac{c_{35}}{\xi_z}\partial_z u_z + \frac{c_{55}}{\xi_z}\partial_z u_x + \frac{c_{55}}{\xi_x}\partial_x u_z\right) + \frac{1}{\xi_z}\partial_z\left(\frac{c_{13}}{\xi_x}\partial_x u_x + \frac{c_{33}}{\xi_z}\partial_z u_z + \frac{c_{35}}{\xi_z}\partial_z u_x + \frac{c_{35}}{\xi_x}\partial_x u_z\right) = 0, \quad (31b)$$

where u_x and u_z are the horizontal and vertical components of particle displacement vector, ρ is the effective density, and c_{ij} are the components of complex-valued and frequency-dependent effective stiffness matrix, ξ_x and ξ_z are the frequency domain PML damping functions.

In time domain, the governing equations are integral differential equations, which require special processing for the convolution operations, resulting in high computational costs. Although the problem can be relieved (mitigated) by memory functions, it still requires high memory requirements. Instead, the governing equations can be straightforwardly solved using FDFD. To efficiently and accurately modelling of seismic wave propagation in fluid saturated fractured porous rock, we solve the second-order heterogeneous governing equations with mixed-grid stencil FDFD method (Jo et al., 1996; Hustedt et al. 2004). The mixed system of governing equations is formulated by combining the classical Cartesian coordinate system (CS) and the 45°-rotated coordinate system (RS):

$$\omega^2\rho u_x + w_1(A_c u_x + B_c u_z) + (1 - w_1)(A_r u_x + B_r u_z) = 0, \quad (32a)$$

$$\omega^2\rho u_z + w_1(C_c u_x + D_c u_z) + (1 - w_1)(C_r u_x + D_r u_z) = 0, \quad (32b)$$

where the optimal averaging coefficient $w_1 = 0.5461$ (Jo et al., 1996). The coefficients A_c, B_c, C_c, D_c and A_r, B_r, C_r, D_r are functions of the damping functions, effective stiffness coefficients and spatial derivative operators and the detailed expressions are given in Appendix A. We follow Hustedt et al., (2004) and Liu et al., (2018) to discretize the derivative operation on the mixed systems using mixed grid stencil. After discretization and arrangement, the mixed system of governing equations can be written in matrix from as

$$\begin{bmatrix} \mathbf{M} + w_1\mathbf{A}_c + (1 - w_1)\mathbf{A}_r & w_1\mathbf{B}_c + (1 - w_1)\mathbf{B}_r \\ w_1\mathbf{C}_c + (1 - w_1)\mathbf{C}_r & \mathbf{M} + w_1\mathbf{D}_c + (1 - w_1)\mathbf{D}_r \end{bmatrix} \begin{bmatrix} \mathbf{u}_x \\ \mathbf{u}_z \end{bmatrix} = \begin{bmatrix} \mathbf{0} \\ \mathbf{0} \end{bmatrix}, \quad (36)$$

where $\mathbf{M}$ denotes the diagonal mass matrix of coefficients $\omega^2\rho$, and blocks $\mathbf{A}_c, \mathbf{B}_c, \mathbf{C}_c, \mathbf{D}_c$ and $\mathbf{A}_r, \mathbf{B}_r, \mathbf{C}_r, \mathbf{D}_r$ form the stiffness matrices for the CS and RS stencils, respectively, and the corresponding coefficients of submatrices are given in

Appendix B.

To improve the modelling accuracy of mixed-grid stencil, the acceleration term $\omega^2\rho$ are approximated using a weighted average over the mixed operator stencil nodes

$$[\omega^2\rho]_{\mathrm{i,j}} \approx \omega^2\left[w_{m1}\rho_{\mathrm{i,j}} + w_{m2}\left(\rho_{\mathrm{i+1,j}} + \rho_{\mathrm{i-1,j}} + \rho_{\mathrm{i,j+1}} + \rho_{\mathrm{i,j-1}}\right) + \frac{(1-w_{m1}-4w_{m2})}{4}\left(\rho_{\mathrm{i+1,j+1}} + \rho_{\mathrm{i-1,j-1}} + \rho_{\mathrm{i-1,j+1}} + \rho_{\mathrm{i+1,j-1}}\right)\right], \quad (37)$$

where the optimal coefficients $w_{m1} = 0.6248$ and $w_{m2} = 0.09381$ are computed by Jo et al. (1996).

In order to assess the FPD effects on seismic response, the similar procedure was adopted in the implementation of elastic modeling by replacing the VLSM with the LFLSM (assuming fluid pressure is equilibrium) or the HFLSM (assuming fluid pressure is unequilibrium).

5.2 Poroelastic modeling based on PLSM

The poroelastic modeling means that we numerically solve the Biot's equations and adopt an explicit implementation of the PLSM across each fracture instead of using the effective media theory. Hence, the poroelastic modeling can naturally deal with the FPD between fracture and background and account for its impact on wave scattering. Although it is difficult to implement an explicit application of PLSM for arbitrary orientated fracture, it is relatively straightforward for horizonal or vertical fracture. In frequency domain, the governing equations for an isotropic poroelastic media in the absent of fractures can be written as (Biot, 1962):

$$\omega^2\rho\mathbf{u} + \omega^2\rho_f\mathbf{w} + \nabla\cdot\boldsymbol{\sigma} = 0, \quad (38a)$$

$$\omega^2\rho_f\mathbf{u} + i\omega\frac{\eta}{\kappa}\mathbf{w} - \nabla P_f = 0, \quad (38b)$$

$$\boldsymbol{\sigma} = [(H_U - 2\mu)\nabla\cdot\mathbf{u} + \alpha M\nabla\cdot\mathbf{w}]\mathbf{I} + \mu(\nabla\mathbf{u} + \nabla\mathbf{u}^{\boldsymbol{T}}), \quad (38c)$$

$$-P_f = \alpha M\nabla\cdot\mathbf{u} + M\nabla\cdot\mathbf{w}. \quad (38d)$$

By discretizing Eqs. (38a)-(38d) using second-order differences, we can obtain:

$$\omega^2\rho u_{x\,\mathrm{i,j}} + \omega^2\rho_f w_{x\,\mathrm{i,j}} + \frac{\sigma_{xx\,\mathrm{i+1,j}} - \sigma_{xx\,\mathrm{i,j}}}{\Delta} + \frac{\sigma_{xz\,\mathrm{i,j+1}} - \sigma_{xz\,\mathrm{i,j}}}{\Delta} = 0, \quad (39a)$$

$$\omega^2\rho u_{x\,\mathrm{i,j}} + \omega^2\rho_f w_{x\,\mathrm{i,j}} + \frac{\sigma_{xx\,\mathrm{i+1,j}} - \sigma_{xx\,\mathrm{i,j}}}{\Delta} + \frac{\sigma_{xz\,\mathrm{i,j+1}} - \sigma_{xz\,\mathrm{i,j}}}{\Delta} = 0, \quad (39b)$$

$$\omega^2\rho_f u_{x\,\mathrm{i,j}} + i\omega\frac{\eta}{\kappa}w_{x\,\mathrm{i,j}} - \frac{P_{f\,\mathrm{i+1,j}} - P_{f\,\mathrm{i,j}}}{\Delta} = 0, \quad (39c)$$

$$\omega^2\rho_f u_{z\,\mathrm{i,j}} + i\omega\frac{\eta}{\kappa}w_{z\,\mathrm{i,j}} - \frac{P_{f\,\mathrm{i,j+1}} - P_{f\,\mathrm{i,j}}}{\Delta} = 0, \quad (39d)$$

$$\sigma_{xx\,\mathrm{i,j}} = H_U\frac{u_{x\,\mathrm{i+1,j}} - u_{x\,\mathrm{i,j}}}{\Delta} + (H_U - 2\mu)\frac{u_{z\,\mathrm{i,j+1}} - u_{z\,\mathrm{i,j}}}{\Delta} + \alpha M\left(\frac{w_{x\,\mathrm{i+1,j}} - w_{x\,\mathrm{i,j}}}{\Delta} + \frac{w_{z\,\mathrm{i,j+1}} - w_{z\,\mathrm{i,j}}}{\Delta}\right), \quad (39e)$$

$$\sigma_{zz\,\mathrm{i,j}} = (H_U - 2\mu)\frac{u_{x\,\mathrm{i+1,j}} - u_{x\,\mathrm{i,j}}}{\Delta} + H_U\frac{u_{z\,\mathrm{i,j+1}} - u_{z\,\mathrm{i,j}}}{\Delta} + \alpha M\left(\frac{w_{x\,\mathrm{i+1,j}} - w_{x\,\mathrm{i,j}}}{\Delta} + \frac{w_{z\,\mathrm{i,j+1}} - w_{z\,\mathrm{i,j}}}{\Delta}\right), \quad (39f)$$

$$\sigma_{xz\,\mathrm{i,j}} = \mu\left(\frac{u_{x\,\mathrm{i,j+1}} - u_{x\,\mathrm{i,j}}}{\Delta} + \frac{u_{z\,\mathrm{i+1,j}} - u_{z\,\mathrm{i,j}}}{\Delta}\right), \quad (39g)$$

$$-P_f = \alpha M\frac{u_{x\,\mathrm{i+1,j}} - u_{x\,\mathrm{i,j}}}{\Delta} + \alpha M\frac{u_{z\,\mathrm{i,j+1}} - u_{z\,\mathrm{i,j}}}{\Delta} + M\left(\frac{w_{x\,\mathrm{i+1,j}} - w_{x\,\mathrm{i,j}}}{\Delta} + \frac{w_{z\,\mathrm{i,j+1}} - w_{z\,\mathrm{i,j}}}{\Delta}\right). \quad (39h)$$

In the presence of horizonal fracture passing through the numerical cell $(\mathrm{i},\mathrm{j}_0)$, the PLSM can be written as:

$$u_{x\,\mathrm{i},\mathrm{j}_0+1}-u_{x\,\mathrm{i},\mathrm{j}_0}=(Z_T\sigma_{xz})_{\mathrm{i},\mathrm{j}_0}, \tag{40a}$$

$$u_{z\,\mathrm{i},\mathrm{j}_0+1}-u_{z\,\mathrm{i},\mathrm{j}_0}=\left(Z_{N_D}\sigma_{zz}+Z_{N_D}\alpha P_f\right)_{\mathrm{i},\mathrm{j}_0}, \tag{40b}$$

$$w_{z\,\mathrm{i},\mathrm{j}_0+1}-w_{z\,\mathrm{i},\mathrm{j}_0}=-\left(\alpha Z_{N_D}\sigma_{zz}+\frac{\alpha Z_{N_D}}{B}P_f\right)_{\mathrm{i},\mathrm{j}_0}. \tag{40c}$$

Rearrange the Eqs. (39e)-(39h), i.e. use the displacement components to represent the stress components, and superimpose the discrete Eqs. (40a)-(40c), we get the following discrete equations:

$$\frac{u_{x\,\mathrm{i+1},\mathrm{j}_0}-u_{x\,\mathrm{i},\mathrm{j}_0}}{\Delta}=\left[\frac{H_D}{4\mu(H_D-\mu)}\sigma_{xx}+\frac{(2\mu-H_D)}{4\mu(H_D-\mu)}\sigma_{zz}+\frac{2\alpha\mu}{4\mu(H_D-\mu)}P_f\right]_{\mathrm{i},\mathrm{j}_0}, \tag{41a}$$

$$\frac{u_{z\,\mathrm{i},\mathrm{j}_0+1}-u_{z\,\mathrm{i},\mathrm{j}_0}}{\Delta}=\left[\frac{(2\mu-H_D)}{4\mu(H_D-\mu)}\sigma_{xx}+\left[\frac{H_D}{4\mu(H_D-\mu)}+\frac{Z_{N_D}}{\Delta}\right]\sigma_{zz}+\left[\frac{2\alpha\mu}{4\mu(H_D-\mu)}+\frac{\alpha Z_{N_D}}{\Delta}\right]P_f\right]_{\mathrm{i},\mathrm{j}_0}, \tag{41b}$$

$$\frac{u_{x\,\mathrm{i},\mathrm{j}_0+1}-u_{x\,\mathrm{i},\mathrm{j}_0}}{\Delta}+\frac{u_{z\,\mathrm{i+1},\mathrm{j}_0}-u_{z\,\mathrm{i},\mathrm{j}_0}}{\Delta}=\left[\left(\frac{1}{\mu}+\frac{Z_T}{\Delta}\right)\sigma_{xz}\right]_{\mathrm{i},\mathrm{j}_0}, \tag{41c}$$

$$\frac{w_{x\,\mathrm{i+1},\mathrm{j}_0}-w_{x\,\mathrm{i},\mathrm{j}_0}}{\Delta}+\frac{w_{z\,\mathrm{i},\mathrm{j}_0+1}-w_{z\,\mathrm{i},\mathrm{j}_0}}{\Delta}=\left[\frac{2\alpha\mu}{4\mu(H_D-\mu)}\sigma_{xx}+\left(\frac{2\alpha\mu}{4\mu(H_D-\mu)}-\frac{\alpha Z_{N_D}}{\Delta}\right)\sigma_{zz}-\frac{1}{M}\left(\frac{H_U-\mu}{H_D-\mu}+\frac{H_U Z_{N_D}}{\Delta}\right)P_f\right]_{\mathrm{i},\mathrm{j}_0}. \tag{41d}$$

For a numerical cell, if $\mathrm{j}\neq\mathrm{j}_0$, we set $Z_{N_D}=Z_T=0$. By re-injecting Eqs. (41a)-(41d) into the discretized Eqs. (39a)-(39c), we eliminate the stress terms and obtain the compact discretized system of wave equations that contain only the displacement field:

$$\begin{bmatrix}\mathbf{G}_{11} & \mathbf{G}_{12} & \mathbf{G}_{13} & \mathbf{G}_{14}\\ \mathbf{G}_{21} & \mathbf{G}_{22} & \mathbf{G}_{23} & \mathbf{G}_{24}\\ \mathbf{G}_{31} & \mathbf{G}_{32} & \mathbf{G}_{33} & \mathbf{G}_{34}\\ \mathbf{G}_{41} & \mathbf{G}_{42} & \mathbf{G}_{43} & \mathbf{G}_{44}\end{bmatrix}\begin{bmatrix}\mathbf{u}_x\\ \mathbf{u}_z\\ \mathbf{w}_x\\ \mathbf{w}_z\end{bmatrix}=\begin{bmatrix}\mathbf{0}\\ \mathbf{0}\\ \mathbf{0}\\ \mathbf{0}\end{bmatrix}, \tag{42}$$

where blocks $\mathbf{G}_{ij}\ (i,j=1\ldots4)$ form the stiffness matrices of the discretized system of the poroelastic wave equations. The poroelastic modeling based on PLSM will be used to validate the other modeling schemes.

6. Numerical examples

Table1 Physical Properties of the Materials Employed in the Numerical Modeling

Parameters	Background	Fracture	Underlying
Porosity, ϕ	0.15	0.8	0.05
Permeability, κ	0.1 D	100 D	0.01 D
Solid bulk modulus, K_s	36 GPa	36 GPa	36 GPa
Frame bulk modulus, K_m	20.3 GPa	0.055 GPa	30.6 GPa
Frame shear modulus, μ_m	18.6 GPa	0.033 GPa	32.2 GPa
Solid density, ρ_s	2700 kg/m³	2700 kg/m³	2700 kg/m³
Fluid density, ρ_f	1000 kg/m³	1000 kg/m³	1000 kg/m³
Fluid shear viscosity, η_f	0.01 Poise	0.01 Poise	0.01 Poise
Fluid bulk modulus, K_f	2.25 GPa	2.25 GPa	2.25 GPa
Thickness, h		1 mm	

In this section, we apply different numerical modeling schemes on three fractured models to examine the FPD effects on seismic wave scattering. We mainly focus on the amplitudes and phases of the scattered and reflected waves generated by pressure source and shearing source.

6.1 Single horizontal fracture model

Here, we numerically simulate the scattering of seismic waves from a single horizontal fracture embedded in a homogeneous background. The model measures $2000\mathrm{m} \times 1500\mathrm{m}$ with a grid interval 5m (namely, the numerical grids size is 401×301) surrounded by a 200m thick PML boundary. The fracture is located 750m directly below the source $(1000\mathrm{m}, 30\mathrm{m})$, with a 500m horizontal extending. A Ricker wavelet with a central frequency of 35Hz is used as the temporal source excitation. The material properties of the fracture and background are given in Table 1 modified from Nakagawa and Schoenberg (2007) and Barbosa et al. (2016a). For comparison, we present the seismic wavefields obtained using the poroelastic modeling based on PLSM, the viscoelastic modeling based on VLSM, as well as the elastic modeling based on LFLSM and HFLSM. To further study the impact of FPD effects on P- and S-wave, we also apply the pressure source and shearing source in all four schemes, respectively.

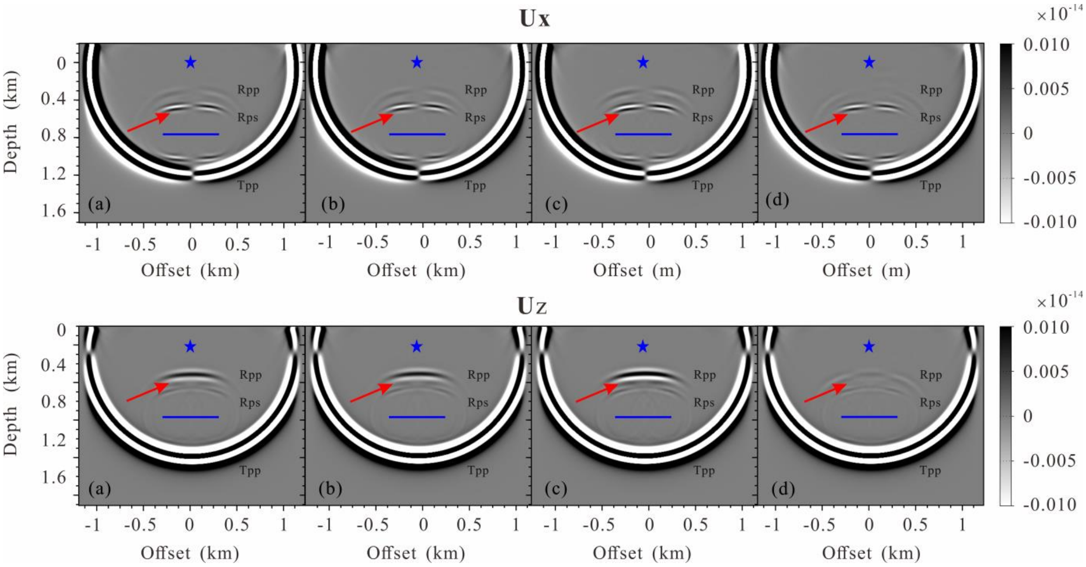

Figure 1: Snapshots of the wavefields components Ux and Uz for a single horizontal fracture model at 280ms due to a P-wave point source: (a) the PLSM based poroelastic modeling, (b) the VLSM based viscoelastic modeling, (c) the LFLSM based elastic modeling and (d) the HFLSM based elastic modeling.

https://doi.org/10.5194/egusphere-2022-1388
Preprint. Discussion started: 2 January 2023

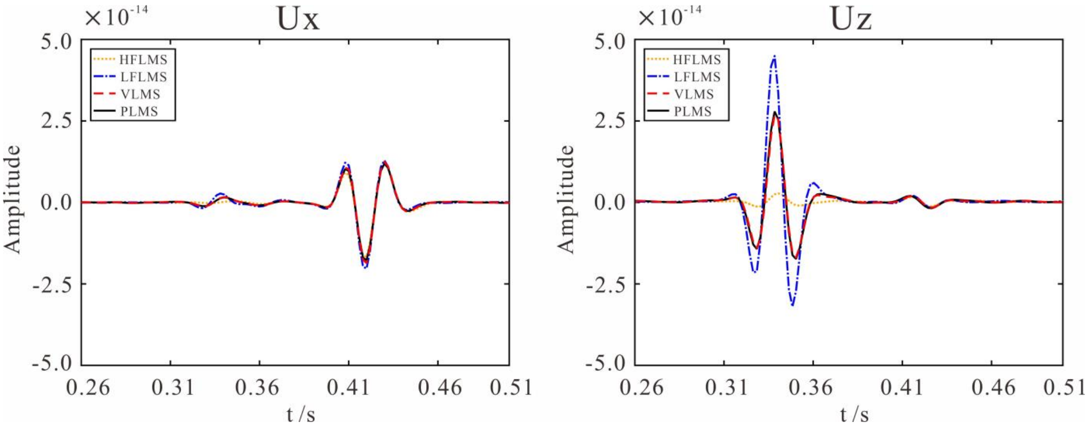

Figure 2: Comparison of 1-D seismograms components Ux and Uz at (1200m, 0m) for a single horizontal fracture model due to a P-wave point source.

Figure 1 shows the 280ms snapshots of the displacement fields for the single horizontal fracture model models with P-wave point source. The displacement fields are calculated by the PLSM-based poroelastic modeling, the VLSM-based viscoelastic modeling, the LFLSM-based elastic modeling and the HFLSM-based elastic modeling, respectively. The asterisk represents the source and the blue line represents the fracture. To make the small scattered wave visible, large amplitude is clipped, thus the transmitted compressional wave (T_{PP}), scattered compressional wave (S_{PP}) and scattered converted wave (S_{PS}) can be seen clearly. Figure 2 present the comparison of 1-D seismograms at (1200m, 0m).

We consider the poroelastic modeling as a reference scenario because it can naturally incorporate the FPD effects. Figure 1 and Figure 2 suggest very good agreement between the S_{PP} amplitude calculated using the PLSM-based and VLSM-based modeling, while the HFLSM-based modeling obviously underestimate the S_{PP} amplitude, and the LFLSM-based modeling overestimate the S_{PP} amplitude. This is to be expected, since the scattering behavior of a fracture is mainly controlled by the stiffness contrast with respect to the background. The HFLSM assumes there is insufficient time for fluid exchange at the fracture interface, the fracture behaves as being sealed and the stiffeness of the saturated fracture is maximal, resulting in an underestimated stiffness contrast between fracture and background. The LFLSM assumes there is enough time for fluid flow between the fracture and background, the deformation of the fracture is maximal, resulting in an overestimated stiffness contrast with background. However, the VLSM derived from poroelastic theory can properly incorporate the FPD effects, leading to a frequency-dependent stiffness contrast equivalent to the PLSM. It can be note that the S_{PP} amplitudes obtained using the LFLSM-based modeling is comparable to that of the PLSM based modeling, because the FPD effects mainly occur at seismic frequencies closer to the low frequency limit. The S_{PP} travel time obtained using the four modeling schemes shows good consistency. Figure 2 also shows that the discrepancy of the S_{PS} amplitudes is almost negligible. Figure 1 and Figure 2 demonstrate that the DLSM-based viscoelastic modeling can appropriately capture the FPD effects on wave scattering of a fluid saturated fracture. However, the two elastic modeling cannot correctly estimate the S_{PP} amplitudes.

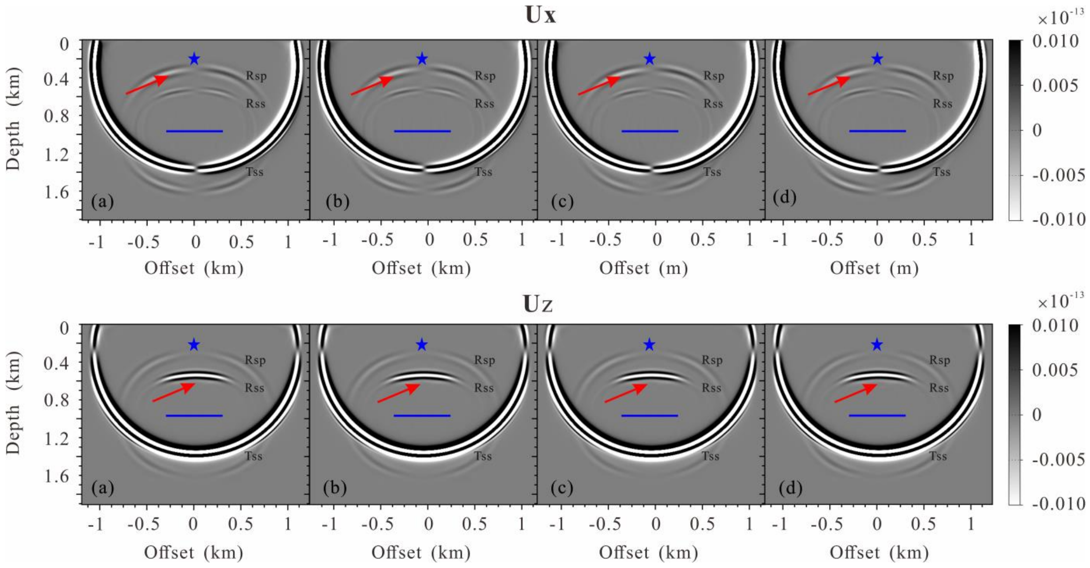

Figure 3: Snapshots of the wavefields components Ux and Uz for a single horizontal fracture model at 280ms due to a S-wave point source: (a) the PLSM based poroelastic modeling, (b) the VLSM based viscoelastic modeling, (c) the LFLSM based elastic modeling and (d) the HFLSM based elastic modeling.

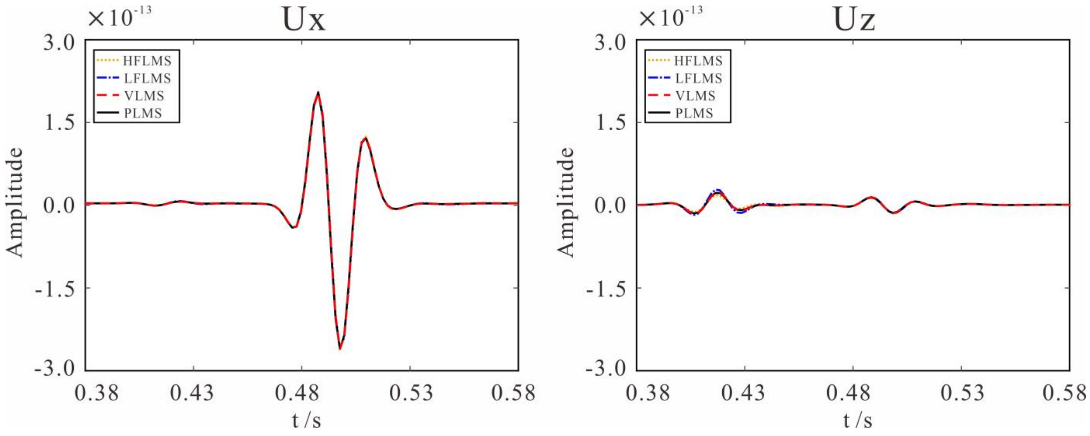

Figure 4: Comparison of 1-D seismograms components Ux and Uz at receiver (1200m, 0m) for a single horizontal fracture model due to a S-wave point source.

Figure 3 shows the 360ms snapshots of the displacement fields for the single horizontal fracture model models with S-wave point source. Figure 4 is the comparison of 1-D seismograms at (1200m,0m). Figure 3 and Figure 4 show that the amplitudes of the calculated S_{SP} and S_{SS} using four modeling schemes have good consistency, indicating that S-wave point source exploration survey is less sensitive to fluids or FDP effects for a single fracture. The scattering behavior is mainly controlled by the drained stiffness contrast between the fracture and the background.

6.2 Fractured reservoir model

In addition to a single fracture, we are more interested in the scattering behavior of discretely distributed fractures system. To

https://doi.org/10.5194/egusphere-2022-1388
Preprint. Discussion started: 2 January 2023

this end, we designed a fractured reservoir model containing a conjugate fracture system (consisting of two sets of mutually perpendicular fractures, as illustrated in Figure 5). The normal spacing and extending of this set of conjugate fractures are 1.768m and 70.7m, respectively. The material properties of the fracture, background (yellow region) and underlying (green region) formation are given in Table 1. The model size, grid interval and source location are the same as those in the previous numerical examples.

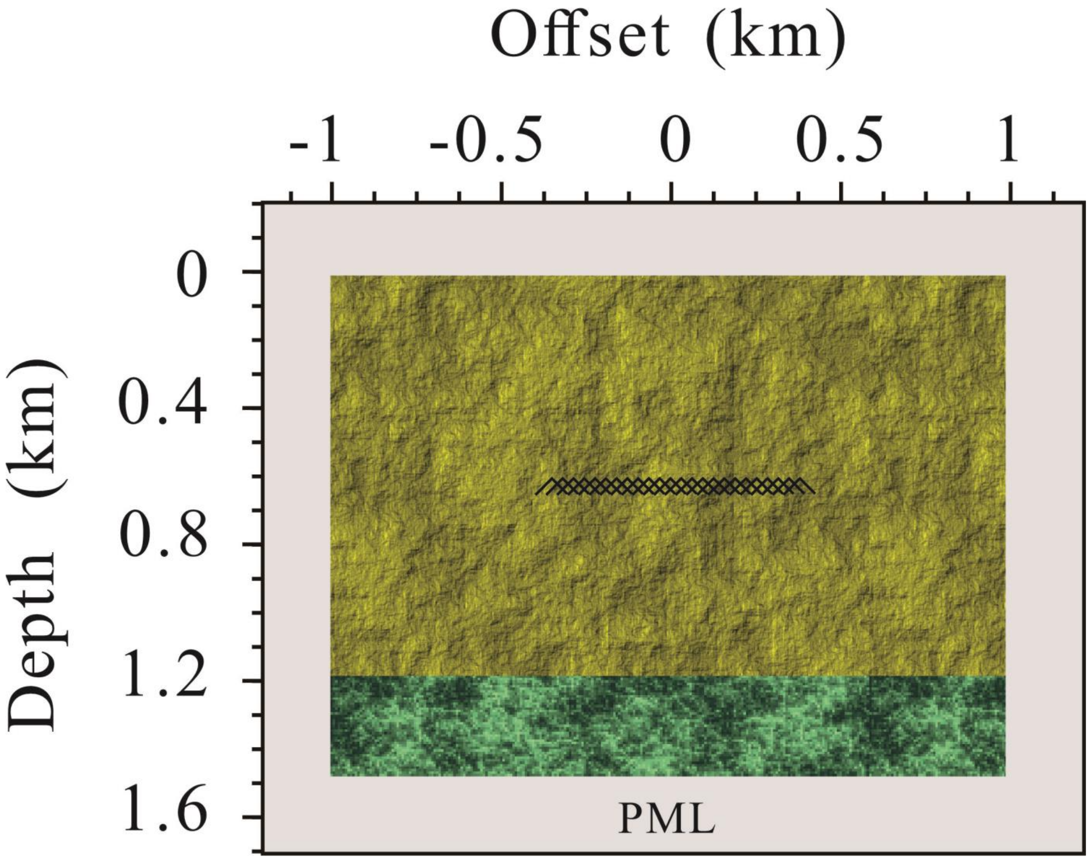

Figure 5: Schematic diagram of the fractured reservoir model I with a conjugate fracture system. The black segments present the fracture system. The normal spacing and extending of each fracture are 1.768m and 70.7m, respectively.

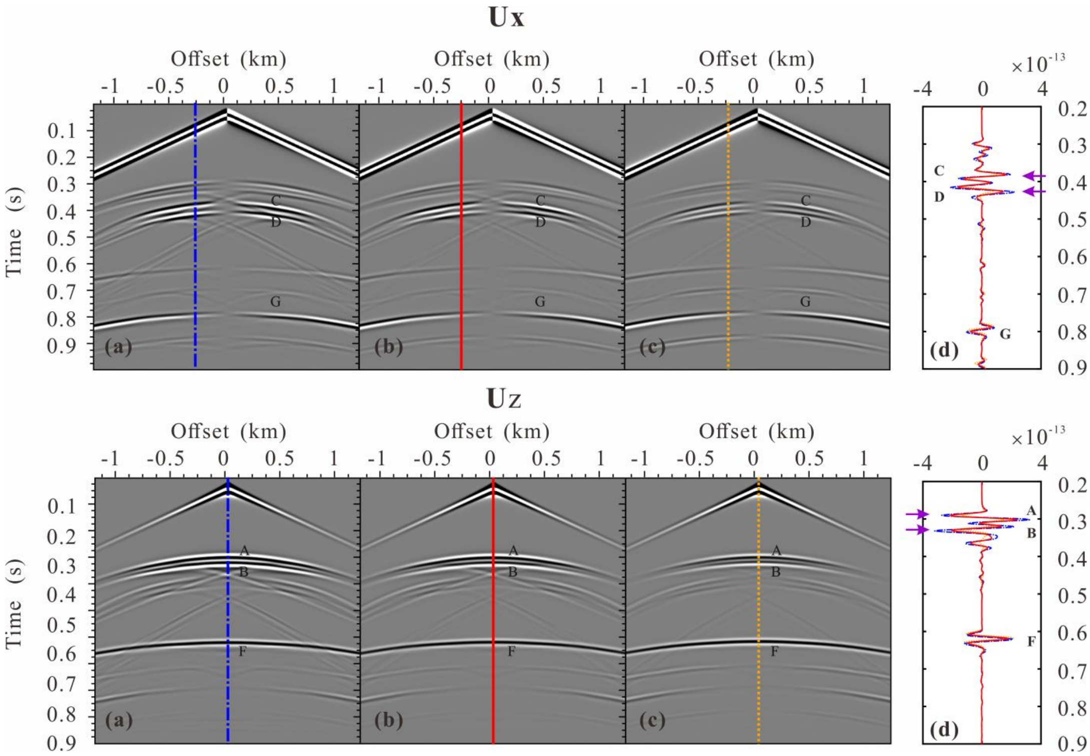

Figure 6: Seismogram components Ux and Uz of the fractured reservoir model I due to a P-wave point source: calculated using (a) the LFLSM, (b) the VLSM, (c) the HFLSM. (d) is the comparison of single trace extracted from the three gathers. A and B are scattered compressional wave from top and bottom, respectively, C and D are scattered converted wave top and bottom, respectively, F and G are reflected compressional wave and converted wave, respectively, E is scattered diffracted wave.

Figure 6 presents the seismograms of fractured reservoir model I for a P-wave point source. The scattered compressional wave (S_{PP}) and scattered converted wave (S_{PS}) from the top and bottom of the fractured reservoir, the reflected compressional wave (R_{PP}), converted wave (R_{PS}) from the underlying formation, diffracted wave at the edge of the fractured reservoir can be clearly identified. Similar to the single fracture case, the amplitude of the S_{PP} from the top of the fractured reservoir obtained by the HFLSM-based modeling is weakest (underestimated), that obtained by LFLSM-based modeling is strongest (overestimated), and that obtained by the VLSM-based modeling is intermediate (accurate). The purple arrows in the Figure 6 (d) indicate that the S_{PP} from the bottom of the fractured reservoir obtained by the LFLSM-based and HFLSM-based modeling has a slightly larger amplitude than that from the top, while the S_{PP} from the bottom of the fractured reservoir obtained by the VLSM-based modeling has a slightly smaller amplitude than that from the top. This is expected, since the VLSM-based modeling scheme can capture the wave attenuation and dispersion due to the FDP effects between the fracture system and background, while the LFLSM and HFLSM represent non-attenuated and non-dispersive elastic processes. However, due to the weak degree of dispersion, the S_{PP} travel time obtained by the three modeling schemes is almost consistent. Figure 6 shows that the amplitudes of the R_{PP} from the underlying formation calculated by the HFLSM-based and LFLSM-based modeling are almost equal, while that calculated by the VLSM-based modeling is attenuated and dispersed. That again indicates the VLSM-based modeling can capture the FPD effects. The S_{PS} and R_{PS} show similar behavior as the S_{PP} and R_{PP}. Figure 6 suggests that the scattered waves from the bottom of the fractured reservoir are attenuated and dispersed by the FPD effects and the reflected waves can retain the relevant attenuation and dispersion information.

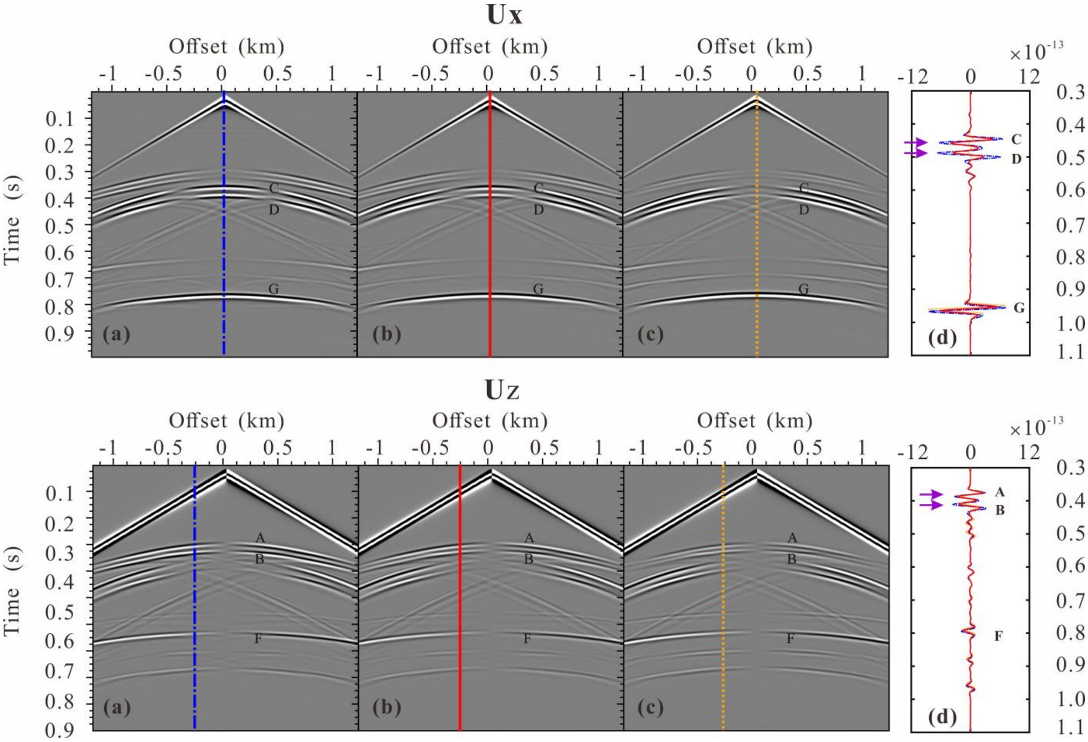

Figure 7: Seismogram components Ux and Uz of the fractured reservoir model I due to a S-wave point source: calculated using (a) the LFLSM, (b) the VLSM, (c) the HFLSM. (d) is the comparison of single trace extracted from the three gathers. A, B are scattered converted SP-wave from top and bottom, respectively, C and D are scattered shear SS-wave from top and bottom, respectively, F and G are reflected converted SP-wave and shear SS-wave, respectively, E is scattered diffracted wave.

Figure 7 presents the seismograms of fractured reservoir model I for a S-wave point source. The scattered converted wave (S_{SP}) and shearing wave (S_{SS}) from the top and bottom of the fractured reservoir, the reflected converted wave (R_{SP}) and shearing wave (R_{SS}) from the underlying formation can be identified in Figure 7. Unlike the case of single horizontal fracture, the FPD effects between a conjugate fracture system and background can attenuate and disperse the S_{PP}, S_{PS}, R_{PP} and R_{PS} for a S-wave point source exploration survey.

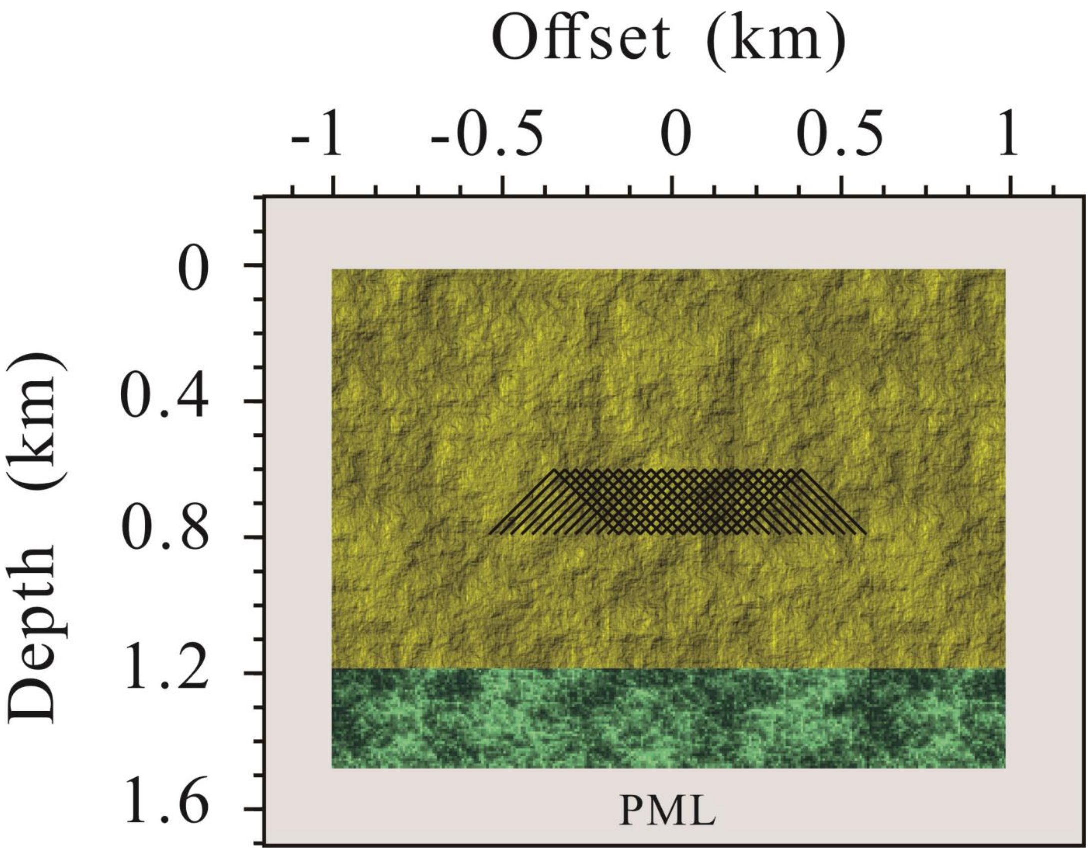

Figure 8: Schematic diagram of the fractured reservoir model II. The normal spacing and extending of each fracture are 1.768m and 282.8m, respectively.

The attenuation and dispersion caused by FDP effects are strongly affected by the thickness of the reservoir. In general, the thicker the fractured reservoir, the more severe attenuation and dispersion of the seismic wave. To demonstrate the strong attenuation and dispersion caused by FDP effect, we modify the fractured model I, increase each fracture to 282.8m without changing other parameters, and obtain a fractured model II. Figure 9 presents the seismograms of fractured reservoir model II for a P-wave point source. Figure 9 shows that the S_{PP} and S_{PS} from the bottom of the fractured reservoir and the R_{PP} and R_{PS} from the underlying formation obtained by the VLSM-based modeling are strongly attenuated and dispersed, proving that the VLSM-based modeling can be captured the FPD effects when seismic waves travel through the fractured reservoir. Figure10 presents the seismograms of the fractured reservoir model II for a S-wave point source. Figure 10 shows that the scattered and reflected waves obtained by VLSM-based modeling are also strongly attenuated and dispersed.

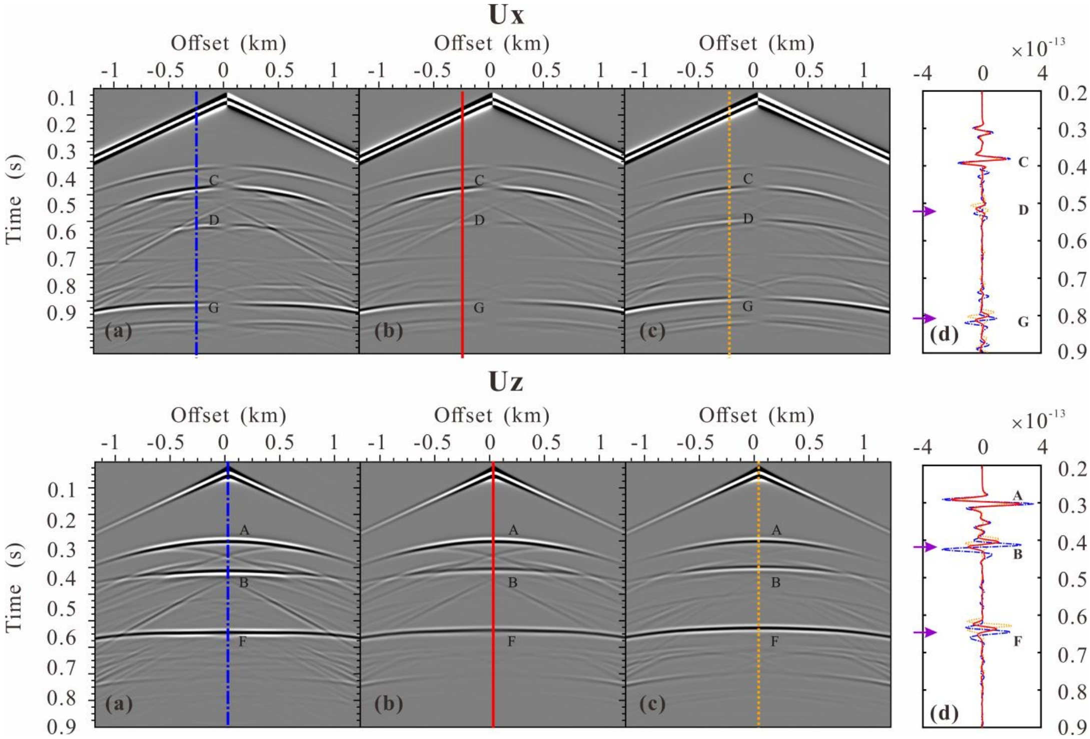

Figure 9: Seismogram components Ux and Uz of the fractured reservoir model II due to a P-wave point source: calculated using (a) the LFLSM, (b) the VLSM, (c) the HFLSM. (d) is the comparison of single trace extracted from the three gathers. The meanings of A, B, C, D, E, F and G are same as those in Figure 9.

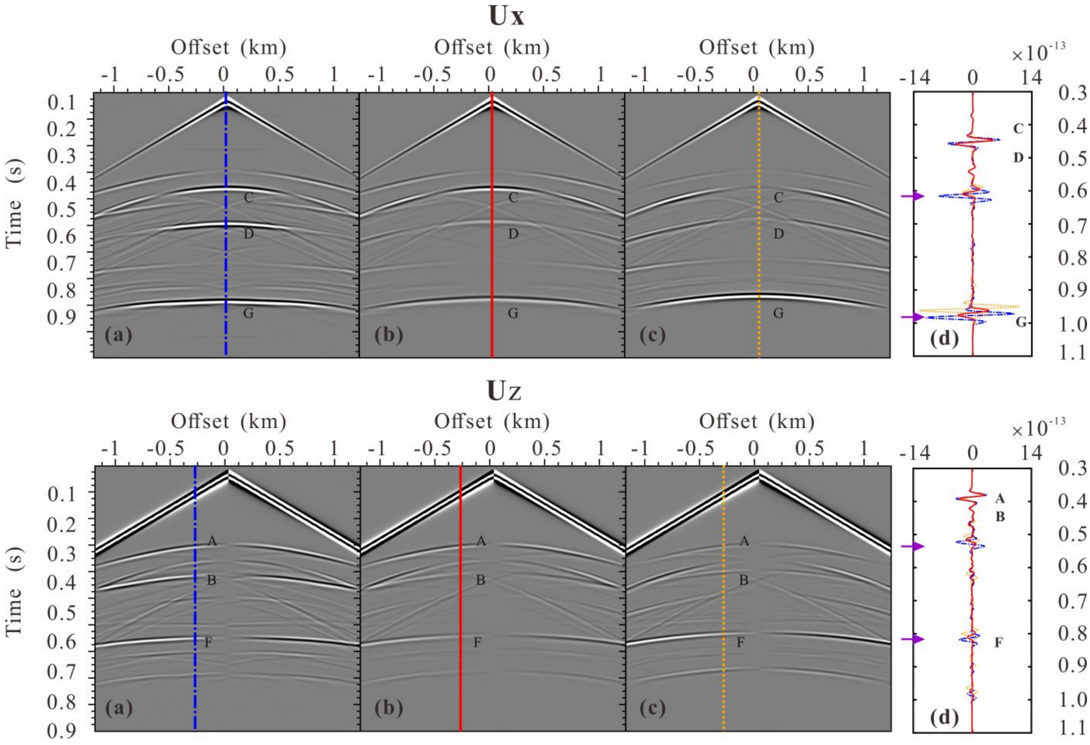

Figure 10: Seismogram components Ux and Uz of the fractured reservoir model I due to a S-wave point source: calculated using (a) the LFLSM, (b) the VLSM, (c) the HFLSM. (d) is the comparison of single trace extracted from the three gathers. The meanings of A, B, C, D, E, F and G are same as those in Figure 10.

6.3 Modified Marmousi model

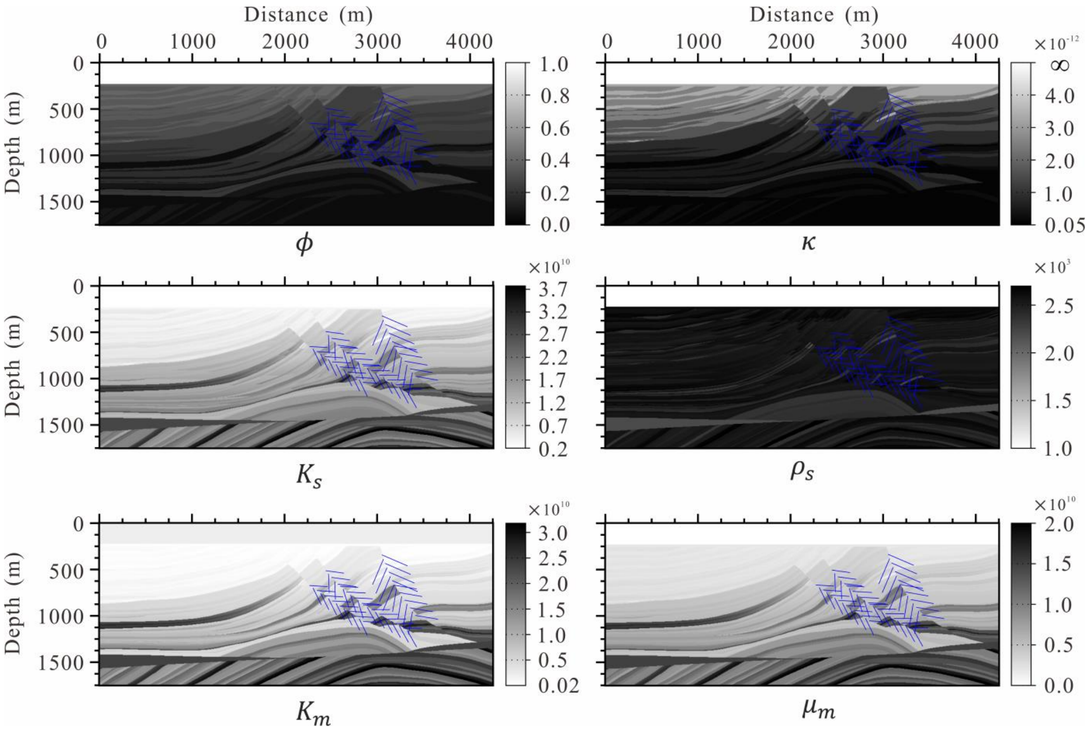

Figure 11: The physical properties and elastic modulus models of the modified Marmousi model.

We test the proposed VLSM-based modeling scheme on a more complex modified Marmousi model. To modify the Marmousi model, we generate a porosity model, permeability model and discrete large-scale fracture system, and transform the original P-wave velocity and density into the fluid saturated bulk and shear modulus of the background by a constant Poisson's ratio 0.5, and finally obtain the grain bulk modulus, the frame bulk and shear modulus of the background through Gassmann equation and empirical formula ($K_m = (1-\phi)^{3/(1-\phi)}K_s$). The input physical properties and elastic modulus models of the modified Marmousi model are present in Figure 11. The fluid density, bulk modulus and viscosity are the same as in Table 1. The model size is 4250m×1750m with grid interval 5m and a 100m thick PML boundary. The source is located at the surface (2125m, 0m). A Ricker wavelet with a central frequency of 25Hz is used as the temporal source excitation.

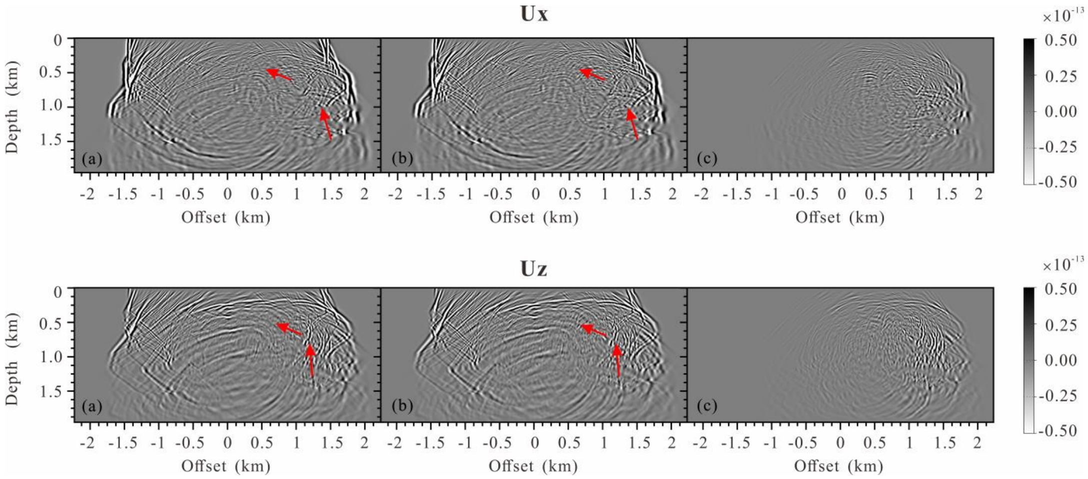

Figure 12: Snapshots of the wavefields components Ux and Uz at 1000ms: (a) the original Marmousi model without fractures, (b) the modified Marmousi model with fractures and (c) the differences.

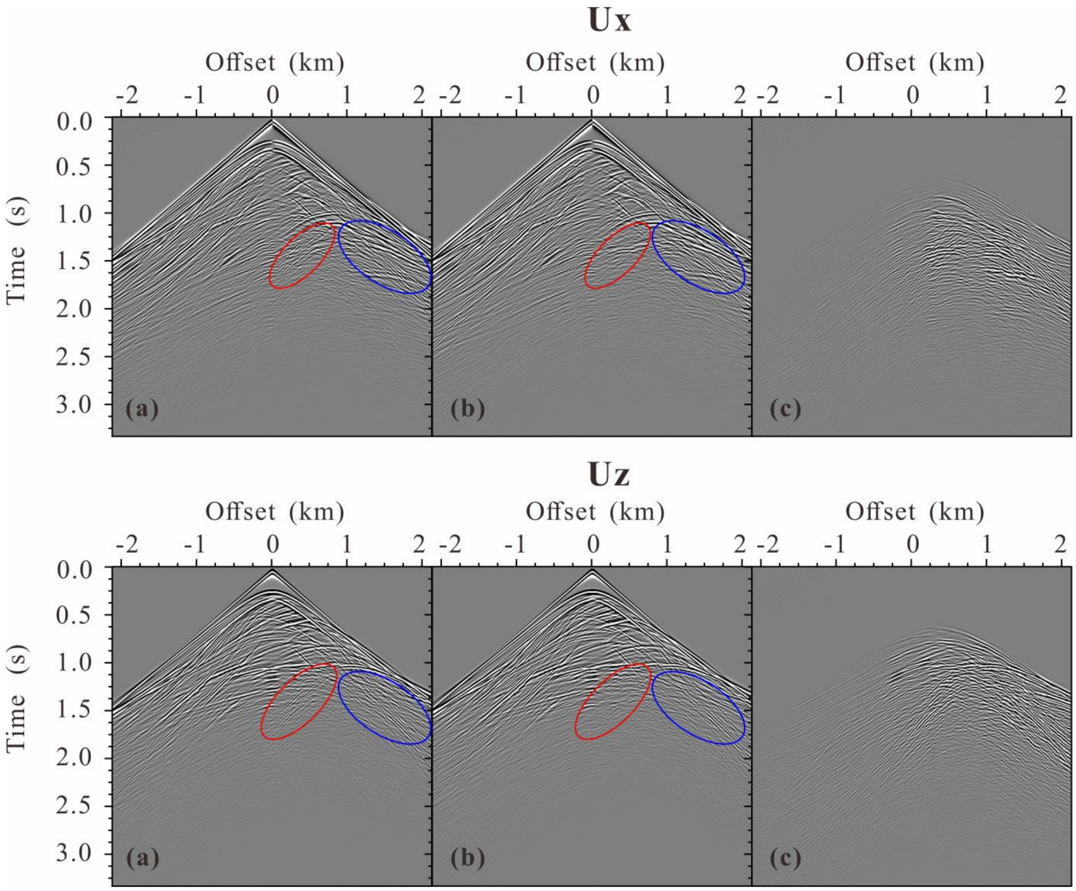

Figure 13: Seismogram components Ux and Uz: (a) the modified Marmousi model with fractures, (b) the original Marmousi model without fractures and (c) the differences.

Figures 12 shows the snapshots of displacement fields at 1000ms. The figure clearly shows the scattered P- and S-waves by the discrete distributed large-scale fractures. The results with such a complex model clearly verify the numerical implementation and the code. We also calculate the seismograms of the displacement shown in Figure 13. The seismograms obtained by our proposed modeling scheme present the scattered seismic waves by the discrete fractures.

7. Conclusions

In this work, we have developed a numerical modeling scheme including FPD effects for discrete distributed large-scale fractures embedded in fluid saturated porous rock. To capture the FPD effects between the fractures and background, the fractures are represented as Barbosa's VLSM with complex-valued and frequency-dependent fracture compliances. Using Coates and Schoenberg's local effective medium theory and Barbosa's VLSM, we derive the effective anisotropic viscoelastic compliances in each spatial discretized cell by superimposing the compliances of the background and the fractures. The local effective governing equations of numerical cells are expressed by the derived effective compliances and discretized by mixed-grid stencil FDFD. The proposed modeling scheme can be used to study the impact of mechanical and hydraulic of fracture properties on seismic scattering.

The numerical results of the single horizontal fracture model with a P-point source valid that the proposed VLSM-based modeling can include the FPD effects and thus accurately estimate the scattered wave of the horizontal fracture. In contrast, the LFLSM-based modeling overestimates the scattered wave and the HFLSM-based modeling underestimates the scattered wave. The numerical results with an S-point source show that the scattered waves off a single horizontal fracture is less sensitive to FDP effects. Due to the differences in fracture orientation, the results of the conjugate fractured reservoir model are quite different from those of the single horizontal fracture model. For both P- and S-point sources, the amplitudes of the scattered waves from the top of the fractured reservoir are affected by the fluid stiffening effects due to the FPD effects. The scattered waves from the bottom of the fractured reservoir are also attenuated and dispersed by the FPD effects in addition to the fluid stiffening effects and the reflected waves can retain the relevant attenuation and dispersion information. The results of the modified Marmousi model clearly show the scattered P- and S-waves by the discrete distributed large-scale fractures and verify the proposed numerical modeling scheme. The proposed numerical modeling scheme is expected not only to improve the estimations of seismic wave scattering from discrete distributed large-scale fractures but can also to improve migration quality and the estimation of fracture mechanical characteristics in inversion.

Appendix A: The coefficients related to spatial derivative operators

We define coefficient vectors $\mathbf{T}_k(k = 1,2,3,4)$ and the derivative operate vector $\mathbf{D}(c)$ as

$$\mathbf{T}_1 = \frac{1}{\xi_x \xi_x}[1 \quad 0 \quad 0 \quad 0],\ \mathbf{T}_2 = \frac{1}{\xi_x \xi_z}[0 \quad 1 \quad 0 \quad 0],\ \mathbf{T}_3 = \frac{1}{\xi_x \xi_z}[0 \quad 0 \quad 1 \quad 0],\ \mathbf{T}_4 = \frac{1}{\xi_z \xi_z}[0 \quad 0 \quad 0 \quad 1], \tag{A-1}$$

$$\mathbf{D}(c) = [\partial_x(c\partial_x) \quad \partial_x(c\partial_z) \quad \partial_z(c\partial_x) \quad \partial_z(c\partial_z)], \tag{A-2}$$

where ξ_x and ξ_z are the PML damping function, c represents effective stiffness. Then, the expression of A_c, B_c, C_c, D_c are written in matrix form:

$$\begin{bmatrix} A_c \\ B_c \\ C_c \\ D_c \end{bmatrix} = \begin{bmatrix} \mathbf{D}(c_{11}) & \mathbf{D}(c_{15}) & \mathbf{D}(c_{15}) & \mathbf{D}(c_{55}) \\ \mathbf{D}(c_{15}) & \mathbf{D}(c_{55}) & \mathbf{D}(c_{13}) & \mathbf{D}(c_{35}) \\ \mathbf{D}(c_{15}) & \mathbf{D}(c_{13}) & \mathbf{D}(c_{55}) & \mathbf{D}(c_{35}) \\ \mathbf{D}(c_{55}) & \mathbf{D}(c_{35}) & \mathbf{D}(c_{35}) & \mathbf{D}(c_{33}) \end{bmatrix} \begin{bmatrix} \mathbf{T}_1 \\ \mathbf{T}_2 \\ \mathbf{T}_3 \\ \mathbf{T}_4 \end{bmatrix}. \tag{A-3}$$

We formulate A_r, B_r, C_r, D_r in a similar way by defining the coefficient vectors $\mathbf{T}_k'(k = 1,2,3,4)$ and $\mathbf{D}'(c)$ as

$$\mathbf{T}_1' = \frac{1}{2\xi_x\xi_x}[1 \quad 1 \quad 1 \quad 1]^T,\ \mathbf{T}_2' = \frac{1}{2\xi_x\xi_z}[-1 \quad 1 \quad -1 \quad 1]^T,$$

$$\mathbf{T}_3' = \frac{1}{2\xi_x\xi_z}[-1 \quad -1 \quad 1 \quad 1]^T,\ \mathbf{T}_4' = \frac{1}{2\xi_z\xi_z}[1 \quad -1 \quad -1 \quad 1]^T, \tag{A-4}$$

$$\mathbf{D}'(c) = [\partial_{x'}(c\partial_{x'}) \quad \partial_{x'}(c\partial_{z'}) \quad \partial_{z'}(c\partial_{x'}) \quad \partial_{z'}(c\partial_{z'})]. \tag{A-5}$$

The expression of A_r, B_r, C_r, D_r are written as

$$\begin{bmatrix} A_r \\ B_r \\ C_r \\ D_r \end{bmatrix} = \begin{bmatrix} \mathbf{D}'(c_{11}) & \mathbf{D}'(c_{15}) & \mathbf{D}'(c_{15}) & \mathbf{D}'(c_{55}) \\ \mathbf{D}'(c_{15}) & \mathbf{D}'(c_{55}) & \mathbf{D}'(c_{13}) & \mathbf{D}'(c_{35}) \\ \mathbf{D}'(c_{15}) & \mathbf{D}'(c_{13}) & \mathbf{D}'(c_{55}) & \mathbf{D}'(c_{35}) \\ \mathbf{D}'(c_{55}) & \mathbf{D}'(c_{35}) & \mathbf{D}'(c_{35}) & \mathbf{D}'(c_{33}) \end{bmatrix} \begin{bmatrix} \mathbf{T}_1' \\ \mathbf{T}_2' \\ \mathbf{T}_3' \\ \mathbf{T}_4' \end{bmatrix}. \tag{A-6}$$

Appendix B: Parsimonious staggered-grid stencil

The nine coefficients of the CS stencil for the submatrix $\mathbf{A}_c$ of Eq. (36):

$$A_{c\,i+1,j} = \frac{c_{11\,i+\frac{1}{2},j}}{\triangle^2\xi_{x\,i}\xi_{x\,i+\frac{1}{2}}},\ A_{c\,i-1,j} = \frac{c_{11\,i-\frac{1}{2},j}}{\triangle^2\xi_{x\,i}\xi_{x\,i-\frac{1}{2}}},\ A_{c\,i,j+1} = \frac{c_{55\,i,j+\frac{1}{2}}}{\triangle^2\xi_{z\,j}\xi_{z\,j+\frac{1}{2}}},\ A_{c\,i,j-1} = \frac{c_{55\,i,j-\frac{1}{2}}}{\triangle^2\xi_{z\,j}\xi_{z\,j-\frac{1}{2}}},$$

$$A_{c\,i,j} = -\frac{c_{11\,i+\frac{1}{2},j}}{\triangle^2\xi_{x\,i}\xi_{x\,i+\frac{1}{2}}} - \frac{c_{11\,i-\frac{1}{2},j}}{\triangle^2\xi_{x\,i}\xi_{x\,i-\frac{1}{2}}} - \frac{c_{55\,i,j+\frac{1}{2}}}{\triangle^2\xi_{z\,i}\xi_{z\,j+\frac{1}{2}}} - \frac{c_{55\,i,j-\frac{1}{2}}}{\triangle^2\xi_{z\,i}\xi_{z\,j-\frac{1}{2}}},\ A_{c\,i+1,j+1} = \frac{c_{15\,i+1,j}+c_{15\,i,j+1}}{4\triangle^2\xi_{x\,i}\xi_{z\,j}},$$

$$A_{c\,i+1,j-1} = -\frac{c_{15\,i+1,j}+c_{15\,i,j-1}}{4\triangle^2\xi_{x\,i}\xi_{z\,j}},\ A_{c\,i-1,j+1} = -\frac{c_{15\,i-1,j}+c_{15\,i,j+1}}{4\triangle^2\xi_{x\,i}\xi_{z\,j}},\ A_{c\,i-1,j-1} = \frac{c_{15\,i-1,j}+c_{15\,i,j-1}}{4\triangle^2\xi_{x\,i}\xi_{z\,j}}. \tag{B-1}$$

The nine coefficients of the RS stencil for the submatrix $\mathbf{A}_r$ of Eq. (36):

$$A_{r\,i+1,j} = \frac{c_{11\,i+\frac{1}{2},j-\frac{1}{2}} - c_{55\,i+\frac{1}{2},j-\frac{1}{2}}}{4\triangle^2\xi_{x\,i}\xi_{z\,j-\frac{1}{2}}} + \frac{c_{11\,i+\frac{1}{2},j+\frac{1}{2}} - c_{55\,i+\frac{1}{2},j+\frac{1}{2}}}{4\triangle^2\xi_{z\,j}\xi_{x\,i+\frac{1}{2}}},\ A_{r\,i-1,j} = \frac{c_{11\,i-\frac{1}{2},j+\frac{1}{2}} - c_{55\,i-\frac{1}{2},j+\frac{1}{2}}}{4\triangle^2\xi_{x\,i}\xi_{z\,j+\frac{1}{2}}} + \frac{c_{11\,i-\frac{1}{2},j-\frac{1}{2}} - c_{55\,i-\frac{1}{2},j-\frac{1}{2}}}{4\triangle^2\xi_{z\,j}\xi_{x\,i-\frac{1}{2}}},$$

$$A_{r\,i,j+1} = \frac{c_{55\,i-\frac{1}{2},j+\frac{1}{2}} - c_{11\,i-\frac{1}{2},j+\frac{1}{2}}}{4\triangle^2\xi_{x\,i}\xi_{z\,j+\frac{1}{2}}} + \frac{c_{55\,i+\frac{1}{2},j+\frac{1}{2}} - c_{11\,i+\frac{1}{2},j+\frac{1}{2}}}{4\triangle^2\xi_{z\,j}\xi_{x\,i+\frac{1}{2}}},\ A_{r\,i,j-1} = \frac{c_{55\,i+\frac{1}{2},j-\frac{1}{2}} - c_{11\,i+\frac{1}{2},j-\frac{1}{2}}}{4\triangle^2\xi_{x\,i}\xi_{z\,j-\frac{1}{2}}} + \frac{c_{55\,i-\frac{1}{2},j-\frac{1}{2}} - c_{11\,i-\frac{1}{2},j-\frac{1}{2}}}{4\triangle^2\xi_{z\,j}\xi_{x\,i-\frac{1}{2}}},$$

$$A_{r\,i,j} = -\frac{c_{11\,i+\frac{1}{2},j-\frac{1}{2}} - 2c_{15\,i+\frac{1}{2},j-\frac{1}{2}} + c_{55\,i+\frac{1}{2},j-\frac{1}{2}}}{4\triangle^2\xi_{x\,i}\xi_{x\,i+\frac{1}{2}}} - \frac{c_{11\,i-\frac{1}{2},j+\frac{1}{2}} - 2c_{15\,i-\frac{1}{2},j+\frac{1}{2}} + c_{55\,i-\frac{1}{2},j+\frac{1}{2}}}{4\triangle^2\xi_{x\,i}\xi_{x\,i-\frac{1}{2}}} - \frac{c_{11\,i+\frac{1}{2},j+\frac{1}{2}} + 2c_{15\,i+\frac{1}{2},j+\frac{1}{2}} + c_{55\,i+\frac{1}{2},j+\frac{1}{2}}}{4\triangle^2\xi_{z\,j}\xi_{z\,j+\frac{1}{2}}} - \frac{c_{11\,i-\frac{1}{2},j-\frac{1}{2}} + 2c_{15\,i-\frac{1}{2},j-\frac{1}{2}} + c_{55\,i-\frac{1}{2},j-\frac{1}{2}}}{4\triangle^2\xi_{z\,j}\xi_{z\,j-\frac{1}{2}}},$$

$$A_{r\,i+1,j+1} = \frac{c_{11\,i+\frac{1}{2},j+\frac{1}{2}} + 2c_{15\,i+\frac{1}{2},j+\frac{1}{2}} + c_{55\,i+\frac{1}{2},j+\frac{1}{2}}}{4\triangle^2\xi_{z\,j}\xi_{z\,j+\frac{1}{2}}},\quad A_{r\,i+1,j-1} = \frac{c_{11\,i+\frac{1}{2},j-\frac{1}{2}} - 2c_{15\,i+\frac{1}{2},j-\frac{1}{2}} + c_{55\,i+\frac{1}{2},j-\frac{1}{2}}}{4\triangle^2\xi_{x\,i}\xi_{x\,i+\frac{1}{2}}},$$

$$A_{r\,i-1,j+1} = \frac{c_{11\,i-\frac{1}{2},j+\frac{1}{2}} - 2c_{15\,i-\frac{1}{2},j+\frac{1}{2}} + c_{55\,i-\frac{1}{2},j+\frac{1}{2}}}{4\triangle^2\xi_{x\,i}\xi_{x\,i-\frac{1}{2}}},\quad A_{r\,i-1,j-1} = \frac{c_{11\,i-\frac{1}{2},j-\frac{1}{2}} + 2c_{15\,i-\frac{1}{2},j-\frac{1}{2}} + c_{55\,i-\frac{1}{2},j-\frac{1}{2}}}{4\triangle^2\xi_{z\,j}\xi_{z\,j-\frac{1}{2}}}. \tag{B-2}$$

The coefficients of the submatrices $\mathbf{B}_c$, $\mathbf{C}_c$, $\mathbf{D}_c$ and $\mathbf{B}_r$, $\mathbf{C}_r$, $\mathbf{D}_r$ can be inferred easily from those of submatrix $\mathbf{A}_c$ and $\mathbf{A}_r$, respectively.

Acknowledgments

This research was financially supported by the National Natural Foundation of China (grant nos. 41874143 and 41574130) and the Key Program of Natural Science Foundation of Sichuan Province (No. 23NSFC0139).

References

Barbosa, N. D., Rubino J. G., Caspari E., and Holliger K.: Extension of the classical linear slipmodel for fluid-saturated fractures: Accounting for fluid pressure diffusion effects, J. Geophys. Res., 122, 1302-1323, doi:10.1002/2016JB013636, 2016a.

Barbosa, N. D., Rubino J. G., Caspari E., Milani M., and Holliger K.: Fluid pressure diffusion effects on the seismic reflectivity of a single fracture, J. Acoust. Soc. Am., 140, 2554-2570, doi:10.1121/1.4964339, 2016b.

Biot, M. A.: Theory of elastic waves in a fluid-saturated porous solid. I. Low frequency range, J. Acoust. Soc. Am., 28, 168-178, doi:10.1121/1.1908239, 1956a.

Biot, M. A.: Theory of elastic waves in a fluid-saturated porous solid. II. High frequency range, J. Acoust. Soc. Am., 28, 179-191, doi:10.1121/1.1908241, 1956b.

Brajanovski, M., Gurevich, B., and Schoenberg, M.: A model for P-wave attenuation and dispersion in a porous medium permeated by aligned fractures, Geophys. J. Int., 163, 372-384, doi:10.1111/j.1365-246X.2005.02722.x, 2005.

Brajanovski, M., Müller T. M., and Gurevich B.: Characteristic frequencies of seismic attenuation due to wave-induced fluid flow in fractured porous media, Geophys. J. Int., 166, 574-578, doi:10.1111/j.1365-246X.2006.03068.x, 2006.

Chapman, M.: Frequency dependent anisotropy due to mesoscale fractures in the presence of equant porosity, Geophys. Prospect., 51, 369-379, doi:10.1046/j.1365-2478.2003.00384.x, 2003.

Coates, R. T. and Schoenberg, M.: Finite-difference modeling of faults and fractures, Geophysics, 60, 1514-1526, doi:10.1190/1.1443884, 1995.

Cui, X. Q., Lines, L. R., and Krebes, E. S.: Seismic modelling for geological fractures, Geophys. Prospect., 2018,157-168, doi:10.1111/1365-2478.12536, 2018.

Dutta, N. C. and Odé, H.: Attenuation and dispersion of compressional waves in fluid-filled porous rocks with partial gas saturation (White Model)-Part I: Biot theory, Geophysics, 44, 1777-1788, doi:10.1190/1.1440938, 1979a.

Dutta, N. C. and Odé, H.: Attenuation and dispersion of compressional waves in fluid-filled porous rocks with partial gas saturation (White Model)-Part II: Results, Geophysics, 44, 1806-1812, doi:10.1190/1.1440939, 1979b.

Gale, J. F. W., Laubach S. E., Olson J. E., Eichhubl P., and Fall A.: Natural fractures in shale: A review and new observations: AAPG Bulletin, 98, 2165-2216, doi:10.1306/08121413151, 2014.

Galvin, R. J. and Gurevich, B.: Frequency-dependent anisotropy of porous rocks with aligned fractures, Geophys. Prospect., 63, 141-150, doi:10.1071/ASEG2003ab016, 2015.

Gassmann, F.: Elastic waves through a packing of spheres, Geophysics, 16, 673-685, doi:10.1190/1.1437718, 1951.

Gavagnin, C., Sanavia, L., and Lorenzis, L. D.: Stabilized mixed formulation for phase-field computation of deviatoric fracture in elastic and poroelastic materials, Comput Mech, 65, 1447-1465, doi:10.1007/s00466-020-01829-x, 2020.

Gelinsky, S. and Shapiro, S. A.: Dynamic-equivalent medium approach for thinly layered saturated sediments, Geophys. J. Int., 128, F1-F4, doi:10.1111/j.1365-246X.1997.tb04086.x, 1997.

Guo J. X., Rubino J. G., Barbosa, N. D., Glubokovskikh, S. G., and Gurevich, B.: Seismic dispersion and attenuation in saturated porous rocks with aligned fractures of finite thickness: Theory and numerical simulations—Part I: P-wave perpendicular to the fracture plane, Geophysics, 83, 49-62, doi:10.1190/geo2017-0065.1, 2017a.

Guo J. X., Rubino J. G., Barbosa, N. D., Glubokovskikh, S. G., and Gurevich, B.: Seismic dispersion and attenuation in saturated porous rocks with aligned fractures of finite thickness: Theory and numerical simulations—Part II: Frequency-dependent anisotropy, Geophysics, 83, 63-71, doi:10.1190/geo2017-0066.1, 2017b.

Gurevich, B., Zyrianov, V. B., and Lopatnikov, S. L.: Seismic attenuation in finely layered porous rocks: Effects of fluid flow and scattering, Geophysics, 62(1), 319-324, doi:10.1190/1.1444133, 1997.

Gurevich, B.: Elastic properties of saturated porous rocks with aligned fractures, J. Geophys. Res., 54, 203-218, doi:10.1016/j.jappgeo.2002.11.002, 2003.

Hustedt, B., Operto S., and Virieux J.: Mixed-grid and staggered-grid finite difference methods for frequency domain acoustic wave modelling, Geophys J Int, 157, 1269-1296, doi:10.1111/j.1365-246X.2004.02289.x, 2004.

Johnson, D. L.: Theory of frequency dependent acoustics in patchy-saturated porous media, J. Acoust. Soc. Am., 110(2), 682-694, doi:10.1121/1.1381021, 2001.

Jo, C.H., Shin, C.S., and Suh, J.H.: An optimal 9-point, finite-difference, frequency-space, 2-D scalar wave extrapolator, Geophysics, 61, 529-537, doi:10.1190/1.1443979, 1996.

Khokhlov, N., Favorskaya, A., Stetsyuk, V., Mitskovets, I.: Grid-characteristic method using Chimera meshes for simulation of elastic waves scattering on geological fractured zones, J. Comput. Phys., 446, 110637, doi:10.1016/j.jcp.2021.110637, 2021.

Krzikalla, F. and Müller T. M.: Anisotropic P-SV-wave dispersion and attenuation due to inter-layer flow in thinly layered porous rocks, Geophysics, 76, WA135-WA145, doi:10.1190/1.3555077, 2011.

Kudarova, A. M., Karel, V. D., and Guy D.: An effective anisotropic poroelastic model for elastic wave propagation in finely layered media, Geophysics, 81, 175-188, doi:10.1190/geo2015-0362.1, 2016.

Liu E. R., Hudson J. A., and Pointer T.: Equivalent medium representation of fractured rock, J. Geophys. Res., 105, 2981-3000, doi:10.1029/1999JB900306, 2000.

Liu, X., Greenhalgh, S., Zhou, B., and Greenhalgh, M.: Frequency-domain seismic wave modelling in heterogeneous porous media using the mixed-grid finite-difference method, Geophys J Int., 216, 34-54, doi:10.1093/gji/ggy410, 2018.

Müller, T. M., Stewart J. T., and Wenzlau, F.: Velocity-saturation relation for partially saturated rocks with fractal pore fluid distribution, Geophys. Res. Lett., 35, L09306, doi:10.1029/2007GL033074, 2008.

Nakagawa, S. and Schoenberg M. A.: Poroelastic modeling of seismic boundary conditions across a fracture, J. Acoust. Soc. Am., 122, 831-847, doi:10.1121/1.2747206, 2007.

Norris, A. N.: Low-frequency dispersion and attenuation in partially saturated rocks, J. Acoust. Soc. Am., 94, 359-370, doi:10.1121/1.407101, 1993.

Oelke, A., Alexandrov, D., Abakumov, I., Glubokovskikh, S., Shigapov, R., Krüger, O. S., Kashtan, B., Troyan, V., and Shapiro, S. A.: Seismic reflectivity of hydraulic fractures approximated by thin fluid layers, Geophysics, 78, 79-87, doi:10.1190/geo2012-0269.1, 2013

Operto, S., Virieux, J., Ribodetti, A., and Anderson J. E.: Finite-difference frequency-domain modeling of viscoacoustic wave propagation in 2D tilted transversely isotropic (TTI) media, Geophysics, 74, 75-95, doi:10.1190/1.3157243, 2009.

Rubino, J. G., Müller T. M., Guarracino L., Milani M., and Holliger K.: Seismoacoustic signatures of fracture connectivity, J. Geophys. Res. Solid Earth., 119, 2252-2271, doi:10.1002/2013JB010567, 2014.

Rubino, J. G., Castromán G. A., Müller T. M., Monachesi L. B., Zyserman F. I., and Holliger K.: Including poroelastic effects in the linear slip theory, Geophysics, 80, A51-A56, doi:10.1190/geo2014-0409.1, 2015.

Sayers, C. M. and Kachanov M.: Microcrack-induced elastic wave anisotropy of brittle rocks, J. Geophys. Res., 100, 4149-4156, doi:10.1029/94JB03134, 1995.

Schoenberg, M. A.: Elastic wave behavior across linear slip interfaces, J. Acoust. Soc. Am., 68, 1516-1521, doi:10.1121/1.385077, 1980.

White, J. E., Mikhahaylova, N. G., and Lyakhovistsky, F. M.: Low-frequency seismic waves in fluid-saturated layered rocks, Izv., Acad. Sci., USSR, Phys. Solid Earth., 11, 654-659, doi:10.1121/1.1995164, 1975.

Zhang, J. F.: Elastic wave modeling in fractured media with an explicit approach, Geophysics, 70, 75-85, doi:10.1190/1.2073886, 2005.